# Reduced Order Models for Thermal Radiative Transfer Problems Based on Moment Equations and Data-Driven Approximations of the Eddington Tensor [*]

Joseph M. Coale[a,b,c], Dmitriy Y. Anistratov[b,d]

[a] *Computational Physics and Methods Group, Los Alamos National Laboratory, Los Alamos, NM*
[b] *Department of Nuclear Engineering, North Carolina State University, Raleigh, NC*
[c] *jmcoale@lanl.gov*
[d] *anistratov@ncsu.edu*

## Abstract

A new group of structure and asymptotic preserving reduced-order models (ROMs) for multidimensional nonlinear thermal radiative transfer (TRT) problems is presented. They are formulated by means of the nonlinear projective approach and data compression techniques. The nonlinear projection is applied to the Boltzmann transport equation (BTE) to derive a hierarchy of low-order moment equations. Approximation of the Eddington tensor that provides exact closure for the system of moment equations is found with projection-based data-driven methodologies. These include the (i) proper orthogonal decomposition (POD), (ii) dynamic mode decomposition (DMD) and (iii) a variant of the DMD. A parameterization is derived for this ROM for the temperature of radiation incoming to the problem domain (the radiation drive temperature). This parameterization is informed from results of a dimensionless study of the TRT problem. Analysis of the ROMs is performed on the classical Fleck-Cummings TRT multigroup test problem in 2D geometry with a radiation-driven Marshak wave. Numerical results are presented to demonstrate the performance of these ROMs for the simulation of evolving radiation and heat waves. Results show these models to be sufficiently accurate for practical computations with rather low-rank representations of the Eddington tensor. As the rank of the approximation is increased, the errors of solutions generated by the ROMs gradually decreases.

*Keywords:* Boltzmann transport equation, quasidiffusion method, variable Eddington factor, proper orthogonal decomposition, dynamic mode decomposition, nonlinear PDEs

## 1. Introduction

The primary mode of energy redistribution in materials that exist at extremely high temperatures is radiative transfer, where energy is transported through the mechanisms of propagation, absorption and emission of photon radiation. Radiative transfer thus plays an

---

essential role in many different physical phenomena that can be found in a wide range of fields including plasma physics, astrophysics, atmospheric and ocean sciences, fire and combustion physics, and high-energy-density physics [1, 2, 3, 4]. The multiphysics models for each of those corresponding phenomena involving radiation transport (e.g. radiation-hydrodynamics problems) are described by complex systems of differential equations. Solving this class of problems is associated with an array of fundamental challenges. The systems of governing equations are generally (i) tightly coupled, (ii) strongly nonlinear, (iii) characterized by multiple scales in space-time, and (iv) high-dimensional.

The Boltzmann transport equation (BTE) describes the propagation of particles in matter. It is an essential part of multiphysics models describing physical systems in which energy redistribution is affected by radiation transport. Its solution depends on 7 independent variables in 3D geometry and typically resides in a higher dimensional space than the other multiphysics equations it becomes coupled to. The BTE drives the dimensionality of these problems, and as such the number of degrees of freedom (DoF) required to describe such physical systems is largely determined by the dimensionality of the BTE solution. Employing a reduced-order model (ROM) for the BTE can thus be an effective means to decrease computational costs associated with multiphysics problems involving radiative transfer.

Of the ROMs that have been previously developed for radiation transport, some of the most well-known include the flux-limited diffusion, $P_1$ and $P_{1/3}$ models [5, 6, 7]. Another group of models are based on the variable Eddington factor method that uses an approximation of the Eddington tensor by means of the first two moments radiation intensity. The Minerbo model is derived by means of a maximum entropy closure for the Eddington tensor. The $M_N$ method applies the maximum entropy closure for a system of $N$ moment equations [8, 9, 10]. Hence, the Minerbo model is the $M_1$ method. Other commonly used models apply Kershaw, Wilson, Livermore closures [11, 12, 13, 14]. The capabilities of these ROMs have been extensively studied and they remain as useful and computationally inexpensive methods for many applications where available computational power is the limiting factor in numerical simulation. However, the accuracy of these models is limited. The generation of more advanced classes of ROMs for these types of problems is currently an active area of research, aimed at the development of models that can produce highly accurate solutions with low computational cost.

In recent times the majority of these research efforts have been focused on the development of data-based models. These models are founded on leveraging the vast amounts of data available from experiments and simulations that have been amassed over the years, with the idea to take advantage of general model-order reduction techniques combined with some given databases to achieve a reduction in dimensionality. Many such techniques are available to choose from [15, 16, 17, 18, 19], some notable examples including: (i) the proper orthogonal decomposition (POD) (a.k.a. principle component analysis (PCA) or the Karhunen-Loève expansion) [20, 21, 22, 23, 24, 25], (ii) the dynamic mode decomposition (DMD) [26, 27, 28, 29], (iii) deep neural networks (DNNs) [30], (iv) the proper generalized decomposition (PGD) [31], (v) balanced truncation [32] and (vi) reduced basis methods [33]. These techniques have seen extensive use in the fluid dynamics community for the modeling of general nonlinear flows [34, 35], linearized flows [36], compressible flows [37], turbulence

[24, 38] and other applications [39, 40]. Naturally the same techniques also have a wide range of applicability in the development of ROMs for particle transport.

Linear particle transport problems have been the subject of development for many such models. The POD and reduced-basis methods have been applied to achieve a reduction in the dimensionality along the angular variable for various neutral particle transport problems [41, 42, 43, 44, 45]. POD-Petrov-Galerkin projection approaches were used to create ROMs for steady-state, parameterized neutral particle transport problems in 1D geometry [46, 47]. The DMD has been applied as a surrogate model to predict neutron populations in subcritical metal systems [48]. Explorations were done with the PGD for separating (i) spatial and energy variables in multigroup neutron diffusion problems [49], (ii) spatial and angular variables for the BTE in 1D slab geometry [50], and (iii) spatial variables for the BTE in 2D Cartesian geometry [51]. A low-rank manifold projection technique has been used to form a ROM for linear time-dependent radiation transport problems [52, 53, 54, 55]. A POD-Galerkin projection based methodology has been developed to perform dimensionality reduction in both space and time for linear dynamical systems and applied to problems of linear Boltzmann transport [56]. Neural networks have been used to (i) obtain data-driven estimations of closures for $P_N$-type systems of moment equations of the linear BTE [57, 58], and (ii) create surrogate models for the 1D linear BTE [59, 60] and the 2D neutron diffusion equation [61].

In addition, development of ROMs for nonlinear problems of radiative transfer has been investigated. The frequency dimension in multigroup $SP_1$ radiative heat transfer calculations has been reduced using a POD-based methodology [62]. POD-Galerkin and trajectory piecewise-linear methods have been used to generate ROMs for spacecraft thermal analysis with a nonlinear radiative heat transfer component [63]. Reduction in frequency dimension was found using an optimization problem to derive few-group models of radiative heat transfer in plasma applications [64]. ROMs for grey nonlinear radiation diffusion problems have been formulated with the PGD [65], POD [66] and modal identification method [67]. POD-based ROMs for radiating fluids have been constructed by applying a linearized estimation of radiative transfer effects based on POD data of non-radiating fluids [68, 69].

Particle transport problems in nuclear reactor-physics applications have also been the subject of data-driven model reduction research efforts. A reduced basis method was applied to pin-by-pin reactor calculations [70]. The PGD has been used to model (i) reactor kinetics [71, 72], and (ii) the neutron flux and cross sections for light water reactors [73]. POD-Galerkin projection was applied to the modeling of steady-state, parameterized molten salt fast reactor problems [74, 75, 76]. POD-Galerkin and DMD-Galerkin approaches have been used to model the neutronics in various reactor type problems with feedback from delayed neutron precursors [77, 78, 79]. A POD-Galerkin projection method has been devised for use with domain-decomposition in reactor simulations [80].

In this paper, ROMs are developed for the fundamental thermal radiative transfer (TRT) problem. This problem is defined by the BTE coupled with the material energy balance (MEB) equation that describes energy exchange between radiation and matter. The TRT problem models a supersonic radiative flow [81], and serves as a useful platform for the development and testing of new computational methodologies. TRT plays an essential role

3

in the evolution of many phenomena contained in high-energy density physics and plasma physics. It can be used to model for instance the important class of supersonic radiation shock experiments [81, 82, 83, 84]. Furthermore, the TRT problem inherits many of the fundamental challenges exhibited by the more general class of radiation hydrodynamics problems.

We present structure and asymptotic preserving ROMs developed by combination of nonlinear projection and data-based techniques of model order reduction. TRT problems in 2D Cartesian geometry are considered. These ROMs are constructed from a set of low-order equations for moments of the specific intensity with data-driven approximate closures. The ROMs are based on the multilevel quasidiffusion (QD) method [85], also known as the variable Eddington factor (VEF) method [86]. This method is in essence a nonlinear method of moments [87, 88, 89, 90, 91, 92, 93, 94, 95, 96, 97]. It is formulated by (i) the high-order BTE and (ii) a hierarchy of low-order QD (LOQD) equations for moments of the radiation intensity. This system is exactly closed through the use of the Eddington (QD) tensor and other linear-fractional factors that are weakly dependent on the BTE solution. Multiphysics equations, e.g. the MEB equation, are coupled to these low-order moment equations on the same dimensional scale as occupied by the multiphysics. This constitutes our initial reduction in dimensionality (with no approximation) and has been shown to give significant advantage compared to other methods in solving multiscale, multiphysical problems.

The multilevel set of LOQD equations coupled with the MEB equation is applied as a basis for model reduction with the use of approximate closures. The hierarchy of multigroup and grey LOQD equations employed by the proposed ROMs are a collection of conservation laws. This leads to preservation of macroscopic behavior of TRT phenomena and yields the foundation for ROMs which reproduce the essential physical structure of the solution as well as its various asymptotic properties. Closure for the multilevel system of LOQD equations is found by means of a data-driven approximation of the Eddington (QD) tensor provided by the POD and DMD. The following analysis shows that ROMs with POD of the Eddington tensor have some advantage compared to those based on DMD. The POD-based approach is applied to develop parameterized ROMs. We consider TRT ROMs that are parameterized over the temperature of radiation incoming to the problem domain (i.e. the radiation drive temperature) using an interpolant between databases. The interpolant is defined based on results from a dimensionless study of the target class of TRT problems, used to identify characteristic scaling relationships between the radiation field and characteristic temperature of radiation.

The remainder of this paper is organized as follows. The TRT problem is defined in Section 2. In Section 3 we formulate the multilevel QD (MLQD) method that is applied as a basis for TRT ROMs. A brief review of the POD and DMD is given in Section 4. The developed class of ROMs for TRT problems in 2D Cartesian geometry based on multilevel moment equations with data-informed closures is formulated in Section 5. Section 6 presents numerical results and analysis of performance of the ROMs on the well-known Fleck-Cummings test problem [98]. Section 7 presents parameterized ROMs for a class of TRT problem. We conclude with a brief discussion in Section 8.

4

## 2. Thermal Radiative Transfer

We consider the TRT problem given by the multigroup BTE [89, 99]

$$\frac{1}{c}\frac{\partial I_g}{\partial t} + \boldsymbol{\Omega} \cdot \boldsymbol{\nabla} I_g + \varkappa_g(T)I_g = \varkappa_g(T)B_g(T), \tag{1}$$
$$\boldsymbol{r} \in \Gamma, \quad \boldsymbol{\Omega} \in \mathcal{S}, \quad g = 1, \ldots, G, \quad t \in [0, t_{end}]$$

with the boundary condition (BC)

$$I_g\big|_{\boldsymbol{r}\in\partial\Gamma} = I_g^{\text{in}}, \quad \boldsymbol{\Omega} \cdot \boldsymbol{e}_n < 0, \tag{2}$$

and the initial condition (IC)

$$I_g\big|_{t=0} = I_g^0, \tag{3}$$

and the MEB equation, which models energy exchange between radiation and matter

$$\frac{\partial \varepsilon(T)}{\partial t} = \sum_{g=1}^{G} \int_{4\pi} \varkappa_g(T)\big(I_g - B_g(T)\big)\ d\Omega, \tag{4}$$

$$T|_{t=0} = T^0. \tag{5}$$

Here $I_g = I_g(\boldsymbol{r}, \boldsymbol{\Omega}, t)$ is the group intensity of radiation, $T = T(\boldsymbol{r}, t)$ is the material temperature, $\varepsilon$ is the material energy density, $\varkappa_g$ is the material opacity for the group $g$, and $B_g$ is the group Planckian function given by

$$B_g(T) = \int_{\nu_{g-1}}^{\nu_g} B(\nu, T)d\nu, \tag{6}$$

where

$$B(\nu, T) = \frac{2}{c^2 h^2} \frac{\nu^3}{e^{\frac{\nu}{T}} - 1}, \tag{7}$$

is the spectral Planckian black-body radiation distribution function. Here $\nu$ and $T$ are measured in eV. $\nu_g$ is the upper boundary of the $g^{\text{th}}$ frequency group and $\nu_0 = 0$. $c$ is the speed of light, $h$ is Planck's constant, $\boldsymbol{r} \in \mathbb{R}^3$ is spatial position, $\boldsymbol{\Omega}$ is the unit vector in the direction of particle motion, $g$ is the frequency group index, $G$ is the number of frequency groups, $t$ is time. We denote $\mathcal{S} = \{\boldsymbol{\Omega} \in \mathbb{R}^3 : |\boldsymbol{\Omega}| = 1\}$, $\Gamma \subset \mathbb{R}^3$ is the spatial domain, $\partial\Gamma$ is the boundary surface of $\Gamma$ and $\boldsymbol{e}_n$ is the outward-facing unit normal vector to $\partial\Gamma$. The TRT problem (1) and (4) neglects photon scattering, material motion and heat conduction.

## 3. The Multilevel Quasidiffusion Method

The MLQD method is formulated by means of a nonlinear projective approach. The BTE is projected in several stages onto a sequence of subspaces to reduce dimensionality of the transport problem and derive a closed hierarchy of low-order equations [88]. This multilevel set of equations for the TRT problem consists of two low-order systems. The 7-dimensional

BTE is projected onto a 5-dimensional subspace by taking its first two angular moments. These equations are written as the multigroup LOQD equations given by [85, 86, 87]

$$\frac{\partial E_g}{\partial t} + \boldsymbol{\nabla} \cdot \boldsymbol{F}_g + c\varkappa_g(T)E_g = 4\pi\varkappa_g(T)B_g(T), \tag{8a}$$

$$\frac{1}{c}\frac{\partial \boldsymbol{F}_g}{\partial t} + c\boldsymbol{\nabla} \cdot (\mathfrak{f}_g E_g) + \varkappa_g(T)\boldsymbol{F}_g = 0, \tag{8b}$$

$$\boldsymbol{e}_n \cdot \boldsymbol{F}_g\big|_{\boldsymbol{r}\in\partial\Gamma} = \left(cC_g\big(E_g - E_g^{\text{in}}\big) + F_g^{\text{in}}\right)\Big|_{\boldsymbol{r}\in\partial\Gamma}, \quad E_g\big|_{t=0} = E_g^0, \quad \boldsymbol{F}_g\big|_{t=0} = \boldsymbol{F}_g^0, \tag{8c}$$

whose unknowns are the multigroup radiation energy density $E_g(\boldsymbol{r},t) = \frac{1}{c}\int_{4\pi} I_g \, d\Omega$ and flux $\boldsymbol{F}_g(\boldsymbol{r},t) = \int_{4\pi} \boldsymbol{\Omega} I_g \, d\Omega$. Note that Eq. (8a) is the group radiation energy balance equation, and Eq. (8b) is the group radiation momentum balance equation. This system is exactly closed via the Eddington (QD) tensor given by

$$\mathfrak{f}_g = \frac{\int_{4\pi} \boldsymbol{\Omega} \otimes \boldsymbol{\Omega} I_g \, d\Omega}{\int_{4\pi} I_g \, d\Omega}. \tag{9}$$

The group boundary factors are defined as

$$C_g = \frac{\int_{\boldsymbol{\Omega}\cdot\boldsymbol{e}_n>0} \boldsymbol{e}_n \cdot \boldsymbol{\Omega} I_g \, d\Omega}{\int_{\boldsymbol{\Omega}\cdot\boldsymbol{e}_n>0} I_g \, d\Omega}\Bigg|_{\boldsymbol{r}\in\partial\Gamma}, \tag{10}$$

and

$$E_g^{\text{in}} = \frac{1}{c}\int_{\boldsymbol{\Omega}\cdot\boldsymbol{e}_n<0} I_g^{\text{in}} \, d\Omega, \quad F_g^{\text{in}} = \int_{\boldsymbol{\Omega}\cdot\boldsymbol{e}_n<0} \boldsymbol{e}_n \cdot \boldsymbol{\Omega} I_g^{\text{in}} \, d\Omega, \tag{11}$$

$$E_g^0 = \frac{1}{c}\int_{4\pi} I_g^0 \, d\Omega, \quad \boldsymbol{F}_g^0 = \int_{4\pi} \boldsymbol{\Omega} I_g^0 \, d\Omega. \tag{12}$$

The multigroup LOQD equations are projected onto a 4-dimensional space by summating them over all frequency groups to obtain the effective grey LOQD equations written as [91]

$$\frac{\partial E}{\partial t} + \boldsymbol{\nabla} \cdot \boldsymbol{F} + c\bar{\varkappa}_E E = c\bar{\varkappa}_B a_R T^4, \tag{13a}$$

$$\frac{1}{c}\frac{\partial \boldsymbol{F}}{\partial t} + c\boldsymbol{\nabla} \cdot (\bar{\mathfrak{f}}E) + \bar{\mathbf{K}}_R \boldsymbol{F} + \bar{\boldsymbol{\eta}}E = 0. \tag{13b}$$

$$\boldsymbol{e}_n \cdot \boldsymbol{F}\big|_{\boldsymbol{r}\in\partial\Gamma} = \left(c\bar{C}\big(E - E^{\text{in}}\big) + F^{\text{in}}\right)\Big|_{\boldsymbol{r}\in\partial\Gamma}, \quad E\big|_{t=0} = E^0, \quad \boldsymbol{F}\big|_{t=0} = \boldsymbol{F}^0, \tag{13c}$$

which solve for the total radiation energy density $E(\boldsymbol{r},t) = \sum_{g=1}^{G} E_g$ and total radiation flux $\boldsymbol{F}(\boldsymbol{r},t) = \sum_{g=1}^{G} \boldsymbol{F}_g$. Here $a_R$ is Stefan's constant. The Eqs. (13a) and (13b) are the

total radiation energy and momentum balance equations, respectively and are exactly closed using the following set of spectrum averaged quantities:

$$\bar{\mathbf{f}} = \frac{1}{\sum_{g=1}^{G} E_g} \sum_{g=1}^{G} \mathbf{f}_g E_g, \quad \bar{\varkappa}_E = \frac{\sum_{g=1}^{G} \varkappa_g E_g}{\sum_{g=1}^{G} E_g}, \quad \bar{\varkappa}_B = \frac{\sum_{g=1}^{G} \varkappa_g B_g}{\sum_{g=1}^{G} B_g}, \tag{14a}$$

$$\bar{\mathbf{K}}_R = \mathrm{diag}\left(\bar{\varkappa}_{R,x},\ \bar{\varkappa}_{R,y},\ \bar{\varkappa}_{R,z}\right), \quad \bar{\varkappa}_{R,\alpha} = \frac{\sum_{g=1}^{G} \varkappa_g |F_{\alpha,g}|}{\sum_{g=1}^{G} |F_{\alpha,g}|}, \quad \alpha = x, y, z, \tag{14b}$$

$$\bar{\boldsymbol{\eta}} = \frac{1}{\sum_{g=1}^{G} E_g} \sum_{g=1}^{G} (\varkappa_g - \bar{\mathbf{K}}_R) \boldsymbol{F}_g. \tag{14c}$$

The boundary and initial conditions for the effective grey system are defined using

$$\bar{C} = \left. \frac{\sum_{g=1}^{G} C_g \left(E_g - E_g^{\mathrm{in}}\right)}{\sum_{g=1}^{G} \left(E_g - E_g^{\mathrm{in}}\right)} \right|_{\boldsymbol{r} \in \partial \Gamma}, \tag{15}$$

$$E^{\mathrm{in}} = \sum_{g=1}^{G} E_g^{\mathrm{in}}, \quad F^{\mathrm{in}} = \sum_{g=1}^{G} F_g^{\mathrm{in}}, \quad E^0 = \sum_{g=1}^{G} E_g^0, \quad \boldsymbol{F}^0 = \sum_{g=1}^{G} \boldsymbol{F}_g^0. \tag{16}$$

Lastly, the MEB equation (4) is cast in effective grey form

$$\frac{\partial \varepsilon(T)}{\partial t} = c \bar{\varkappa}_E E - c \bar{\varkappa}_B a_R T^4 \tag{17}$$

to couple with the effective grey LOQD equations (13). In sum, the MLQD method for TRT problems is formulated with:

1. The high-order multigroup BTE (1) for the group intensity $I_g$,
2. The multigroup LOQD equations for $E_g$ and $\boldsymbol{F}_g$ defined by Eqs. (8),
3. The effective grey problem comprising the effective grey LOQD equations for $E$ and $\boldsymbol{F}$ coupled with the MEB equation for $T$ (Eqs. (13) and (17)).

The components of the group Eddington tensor $\mathbf{f}_g$ and the boundary factor $C_g$ are compressed data of the high-order solution of the BTE (1). These data carry all information about the BTE solution that the hierarchy of the low-order equations (8) and (13) needs to accurately describe radiative transfer physics. In this multilevel system of equations, the high-order BTE (1) can be interpreted as the one that generates the shape function for averaging and calculation of $\mathbf{f}_g$ and $C_g$. The role of the low-order equations is to generate the moments of the transport solution and communicate with the MEB equation as an element of a multiphysics model.

7

# 4. Projection of Data onto Low-Rank Subspaces Using the POD and DMD

## 4.1. Proper Orthogonal Decomposition

Let $\{\boldsymbol{a}^n\}_{n=0}^N$ be a set of data-vectors $\boldsymbol{a} \in \mathbb{R}^d$ such that $\boldsymbol{a}^n = \boldsymbol{a}(t^n)$ for $n = 0, \ldots, N$ at some set of instances $\{t^n\}_{n=0}^N$, which cover the time interval of the problem with $t^0 = 0$ and $t^N = t_{end}$. The POD seeks an orthonormal basis $\{\boldsymbol{u}_1, \boldsymbol{u}_2, \ldots, \boldsymbol{u}_k\}$ onto which the set of zero-mean data $\{\hat{\boldsymbol{a}}^n\}_{n=0}^N$, defined as

$$\hat{\boldsymbol{a}}^n = \boldsymbol{a}^n - \bar{\boldsymbol{a}}, \quad \bar{\boldsymbol{a}} = \frac{1}{N+1} \sum_{n=0}^N \boldsymbol{a}^n \tag{18}$$

can be projected in a way that optimally captures the energy associated with the given data set [23]. This optimality condition amounts to finding the projection of $\{\boldsymbol{a}^n\}_{n=0}^N$ onto $\mathrm{span}\{\bar{\boldsymbol{a}}, \boldsymbol{u}_1, \boldsymbol{u}_2, \ldots, \boldsymbol{u}_k\}$ with minimal error in the Frobenius norm. The rank-$k$ POD expansion of the dataset $\{\boldsymbol{a}^n\}_{n=0}^N$ is written as

$$\boldsymbol{a}^n \approx \bar{\boldsymbol{a}} + \sum_{i=1}^k \alpha_i^n \boldsymbol{u}_i, \tag{19}$$

where the coefficients are given by

$$\alpha_i^n = \langle \hat{\boldsymbol{a}}^n, \boldsymbol{u}_i \rangle, \quad n = 0, \ldots, N, \quad i = 1, \ldots, k. \tag{20}$$

Let us define the matrices $\mathbf{A} \in \mathbb{R}^{d \times (N+1)}$ whose columns are given by the vectors $\{\hat{\boldsymbol{a}}^n\}_{n=0}^N$. The thin (reduced) singular value decomposition (SVD) of $\mathbf{A}$ is

$$\mathbf{A} = \mathbf{U}\mathbf{S}\mathbf{V}^\top, \tag{21}$$

where $\mathbf{U} \in \mathbb{R}^{d \times r}$ and $\mathbf{V} \in \mathbb{R}^{(N+1) \times r}$ hold the first $r$ left and right singular vectors of $\mathbf{A}$ in their columns, respectively, and $\mathbf{S} \in \mathbb{R}^{r \times r}$ holds the $r$ nonzero singular values of $\mathbf{A}$ along its diagonal in descending order, where $r = \mathrm{rank}(\mathbf{A})$. The POD basis vectors are found as the first $k$ columns of $\mathbf{U}$ and the projection coefficients are $\alpha_i^n = v_{n,i}\sigma_i$, where $\sigma_i$ is the $i^{\text{th}}$ singular value of $\mathbf{A}$ and $v_{n,i}$ is the $(n,i)^{\text{th}}$ element of $\mathbf{V}$. An efficient compression of $\mathbf{A}$ is then constructed with the rank-$k$ truncated SVD (TSVD) of $\mathbf{A}$

$$\mathbf{A} \approx \mathbf{A}_k = \mathbf{U}_k \mathbf{S}_k \mathbf{V}_k^\top, \quad k \leq r \tag{22}$$

where $\mathbf{U}_k \in \mathbb{R}^{d \times k}$ and $\mathbf{V}_k \in \mathbb{R}^{(N+1) \times k}$ hold the first $k$ left and right singular vectors of $\mathbf{A}$ in their columns, respectively, and $\mathbf{S}_k \in \mathbb{R}^{k \times k}$ holds the first $k$ singular values of $\mathbf{A}$ along its diagonal in descending order. $\mathbf{A}_k$ is actually the orthogonal projection of $\mathbf{A}$ onto $\{\boldsymbol{u}_i\}_{i=1}^k$, written as $\mathbf{A}_k = \mathbf{U}_k \mathbf{U}_k^\top \mathbf{A}$. The error introduced by this orthogonal projection is given by [100]

$$\|\mathbf{A} - \mathbf{U}_k \mathbf{U}_k^\top \mathbf{A}\|_F^2 = \sum_{i=k+1}^r \sigma_i^2 \tag{23}$$

8

and

$$\|\mathbf{A} - \mathbf{U}_k \mathbf{U}_k^\top \mathbf{A}\|_2 = \sigma_{k+1}. \tag{24}$$

The relative error of the POD approximation in the Frobenius norm is therefore

$$\xi^2 = \frac{\|\mathbf{A} - \mathbf{A}_k\|_F^2}{\|\mathbf{A}\|_F^2} = \frac{\sum_{i=k+1}^r \sigma_i^2}{\sum_{i=1}^r \sigma_i^2}. \tag{25}$$

$(1 - \xi^2)$ can be interpreted as the ratio of energy encompassed by the first $k$ POD modes to the total energy comprised by all POD modes of the given data [38]. Thus the interpretation of $\xi^2$ is the relative amount of energy that has been truncated from the full POD basis by using only the first $k$ POD modes. When the POD is performed, we choose some desired value for $\xi$ and find the rank $k$ that satisfies the following expression

$$k = \min \left\{ j \ : \ \frac{\sum_{i=j+1}^r \sigma_i^2}{\sum_{i=1}^r \sigma_i^2} \leq \xi^2 \right\} \tag{26}$$

### 4.2. Dynamic Mode Decomposition

We consider the case when all time instances $\{t^n\}_{n=0}^N$ are uniformly spaced such that

$$t^{n+1} = t^n + \Delta t, \quad n = 0, \ldots, N-1. \tag{27}$$

Note that DMD methods have been developed to allow for non-uniform sampling of time steps [101, 102]. The DMD constructs the best-fit linear operator $\mathbf{B}$ to the data $\{\boldsymbol{a}^n\}_{n=0}^N$, generating the following dynamic system:

$$\frac{d\tilde{\boldsymbol{a}}(t)}{dt} = \mathbf{B}\tilde{\boldsymbol{a}}(t), \tag{28}$$

whose solution $\tilde{\boldsymbol{a}}(t)$ approximates $\boldsymbol{a}(t)$ and is given by

$$\tilde{\boldsymbol{a}}(t) = \sum_{i=1}^k \beta_i \boldsymbol{\varphi}_i e^{\omega_i t}, \tag{29}$$

where $(\boldsymbol{\varphi}_i, \omega_i)$ are the eigenpairs of $\mathbf{B}$ and $\{\beta_i\}_{i=1}^k$ is some set of coefficients. The eigenpairs $(\boldsymbol{\varphi}_i, \omega_i)$ are calculated with the following orbital data matrices

$$\mathbf{X} = [\boldsymbol{a}^0 \ \boldsymbol{a}^1 \ \ldots \ \boldsymbol{a}^{N-1}] \in \mathbb{R}^{d \times N}, \quad \hat{\mathbf{X}} = [\boldsymbol{a}^1 \ \boldsymbol{a}^2 \ \ldots \ \boldsymbol{a}^N] \in \mathbb{R}^{d \times N}, \tag{30}$$

which define $\tilde{\mathbf{B}} = \hat{\mathbf{X}}\mathbf{X}^+$ as the closest approximation to $\mathbf{B}$ in the Frobenius norm given the dataset $\{\boldsymbol{a}^n\}_{n=0}^N$, where + signifies the Moore-Penrose pseudo inverse [100]. The eigenpairs of $\tilde{\mathbf{B}}$, written as $(\tilde{\boldsymbol{\varphi}}_i, \lambda_i)$, are closely related to the eigenpairs of $\mathbf{B}$ [28] and each eigenvector $\boldsymbol{\varphi}_i$ can be calculated from the corresponding reduced eigenvector $\tilde{\boldsymbol{\varphi}}_i$. The pairs $(\boldsymbol{\varphi}_i, \lambda_i)$ can construct $\tilde{\boldsymbol{a}}(t)$ at the specific points $\{t^n\}_{n=0}^N$ used to define the dataset (30) as

$$\tilde{\boldsymbol{a}}(t^n) = \sum_{i=1}^k \beta_i \boldsymbol{\varphi}_i (\lambda_i)^n, \quad n = 0, \ldots, N. \tag{31}$$

9

Note that Eq. (31) cannot find $\tilde{\boldsymbol{a}}(t)$ for $t \notin \{t^n\}_{n=0}^N$ without some attached interpolant in time. The continuous-in-time DMD expansion (29) is found with the transformation $\omega_i = \frac{\ln(\lambda_i)}{\Delta t}$. The pairs $(\boldsymbol{\varphi}_i, \lambda_i)$ are called DMD modes and eigenvalues and are in practice calculated via the projected linear operator $\tilde{\mathbf{B}}_k = \mathbf{U}_k^\top \tilde{\mathbf{B}} \mathbf{U}_k$, whose eigenpairs are written as $(\tilde{\boldsymbol{\varphi}}_i^{(k)}, \lambda_i)$. Here $\mathbf{U}_k$ holds the left singular vectors of $\mathbf{X}$ in its columns. Note that the eigenvalues of $\tilde{\mathbf{B}}_k$ are the DMD eigenvalues. The process of calculating the eigenpairs $(\boldsymbol{\varphi}_i, \lambda_i)$ is outlined in Algorithm 1 [28].

---

**Algorithm 1:** Algorithm for computing DMD modes and eigenvalues [28]

Input: solution data $\{\boldsymbol{a}^n\}_{n=0}^N$ and $\xi \in [0, 1]$

1. Construct orbital data matrices $\mathbf{X}, \hat{\mathbf{X}} \leftarrow \{\boldsymbol{a}^n\}_{n=0}^N$ via Eq. (30)
2. Compute TSVD $\mathbf{X} \approx \mathbf{U}_k \mathbf{S}_k \mathbf{V}_k^\top$ with $k \leq \text{rank}(\mathbf{X})$ satisfying Eq. (26) using $\xi$
3. Compute reduced DMD matrix $\tilde{\mathbf{B}}_k = \mathbf{U}_k^\top \hat{\mathbf{X}} \mathbf{V}_k \mathbf{S}_k^{-1}$
4. Find eigenpairs $\{(\tilde{\boldsymbol{\varphi}}_i^{(k)}, \lambda_i)\}_{i=1}^k$ of $\tilde{\mathbf{B}}_k$
5. Compute DMD modes:
    - (Exact DMD) $\boldsymbol{\varphi}_i \leftarrow \frac{1}{\lambda_i} \hat{\mathbf{X}} \mathbf{V}_k \mathbf{S}_k^{-1} \tilde{\boldsymbol{\varphi}}_i^{(k)}, \quad \lambda_i \neq 0, \quad i = 1, \dots, k$
    - (Projected DMD) $\hat{\boldsymbol{\varphi}}_i \leftarrow \mathbf{U}_k \tilde{\boldsymbol{\varphi}}_i^{(k)}, \quad i = 1, \dots, k$

Output: DMD modes $\{\boldsymbol{\varphi}_i\}_{i=1}^k$ or $\{\hat{\boldsymbol{\varphi}}_i\}_{i=1}^k$ and DMD eigenvalues $\{\lambda_i\}_{i=1}^k$

---

In Algorithm 1 there are two types of DMD modes that can be calculated: (i) *exact* DMD modes and (ii) *projected* DMD modes. In practice the *exact* DMD modes are preferred, as they can be shown to be the eigenvectors of the linear operator $\mathbf{B}$ that lie in the image of $\hat{\mathbf{X}}$. The *projected* DMD modes have been shown to be simply the projection of the exact modes onto the image of $\mathbf{X}$ [28]. Because the *exact* DMD modes are generally regarded as the default in literature we find it important to note that for the ROMs developed in this paper, when the DMD is invoked we actually use the *projected* modes.

The projected DMD modes ($\hat{\boldsymbol{\varphi}}_i$) were used in the original formulation of the DMD, which can be interpreted as a method that approximates the last data-vector as a linear combination of all former vectors, i.e.

$$\boldsymbol{a}^N = \sum_{n=0}^{N-1} c_n \boldsymbol{a}^n + \varsigma, \tag{32}$$

where $c_n$ are coefficients and $\varsigma$ is the residual incurred by the DMD approximation [103]. It comes naturally then, that when the exact DMD modes are used instead of the projected DMD modes, the DMD can be interpreted as approximating the *first* data-vector as a linear combination of all latter vectors,

$$\boldsymbol{a}^0 = \sum_{n=1}^{N} c_n \boldsymbol{a}^n + \hat{\varsigma}, \tag{33}$$

since the exact DMD modes lie in the image of $\hat{\mathbf{X}}$. This effective 'shift' of the DMD residual to the first data-vector can come at a large cost to the time-dependent problems we consider. The initial transients of these problems are more rapidly evolving than the later ones and are less likely to be well captured by an expansion in the later solutions. It is with this in mind that we choose to utilize the projected DMD modes in this paper when applying the expansion (29).

### 4.3. Equilibrium-Subtracted DMD

A variant of the DMD is also considered for model-order reduction purposes which we will refer to as the equilibrium-subtracted DMD, or DMD-E. The DMD-E differs from the DMD by constructing the linear operator $\mathbf{B}$ to fit the equilibrium-subtracted data $\{\check{\boldsymbol{a}}^n\}_{n=0}^{N'}$, where $\check{\boldsymbol{a}}^n = \boldsymbol{a}^n - \boldsymbol{a}_e$ and $\boldsymbol{a}_e$ is an equilibrium solution vector [103, 104] for the given problem. Note that the DMD-E in the case when $\boldsymbol{a}_e = \bar{\boldsymbol{a}}$ (ref. Eq. (18)) is equivalent to the Fourier expansion of the data [103]. The same algorithm used for the DMD (Alg. 1) is used to calculate the DMD-E eigenvectors and modes, only replacing $\{\boldsymbol{a}^n\}_{n=0}^N$ with $\{\check{\boldsymbol{a}}^n\}_{n=0}^{N'}$. The original function $\boldsymbol{a}(t)$ is reconstructed through the following expansion, similar to Eq. (29), as

$$\boldsymbol{a}(t) \approx \boldsymbol{a}_e + \sum_{i=1}^k \beta_i \hat{\boldsymbol{\varphi}}_i e^{\omega_i t}. \tag{34}$$

The vector $\boldsymbol{a}_e$ is chosen from any equilibrium solution of the underlying system that determines $\boldsymbol{a}(t)$ [104]. The time-dependent TRT problems under consideration here possess a steady-state solution that is approached as $t \to \infty$. The most natural choice for this application is then to let $\boldsymbol{a}_e = \lim_{t\to\infty} \boldsymbol{a}(t)$. In this study $\boldsymbol{a}_e = \boldsymbol{a}(t^N)$ is used to approximate the steady-state solution, so that $N' = N - 1$ and the equilibrium subtracted data is

$$\check{\boldsymbol{a}}^n = \boldsymbol{a}^n - \boldsymbol{a}^N, \quad n = 0, \ldots, N - 1. \tag{35}$$

## 5. Multilevel Moment Equations with Data-Driven Closures

In this study, we develop ROMs for TRT on the basis of the hierarchy of LOQD moment equations (8) and (13) coupled with the MEB equation (17) where the Eddington tensor is approximated by data-driven techniques. This forms a class of ROMs henceforth referred to as data-driven Eddington tensor (DET) ROMs. By nature these ROMs require data for the Eddington tensor that is known a-priori. This Eddington tensor data is generated as the full-order model (FOM) solution (Eqs. (1), (8), (13) and (17)) for some set of base-case (reference) problems the parameters of which cover a desired range. Given this set of data, the chosen data-driven functional must then approximate discrete grid functions of the Eddington tensor and LOQD boundary factors. These grid functions will vary based on the scheme used to discretize the multigroup LOQD system in space. We consider a $2^{\text{nd}}$-order finite-volumes scheme [105], confined to orthogonal spatial grids in 2D Cartesian geometry, denoting the number of cells in the $x$- and $y$- directions as $X$ and $Y$ respectively.

Vectors of each component of the group Eddington tensor and boundary factors are constructed at every $n^{\text{th}}$ time step over the entire spatial grid as

$$\mathfrak{f}^n_{\alpha\beta,g,\gamma} \in \mathbb{R}^{D_\gamma}, \quad \gamma = v, h, c, \quad \alpha, \beta = x, y, \tag{36a}$$
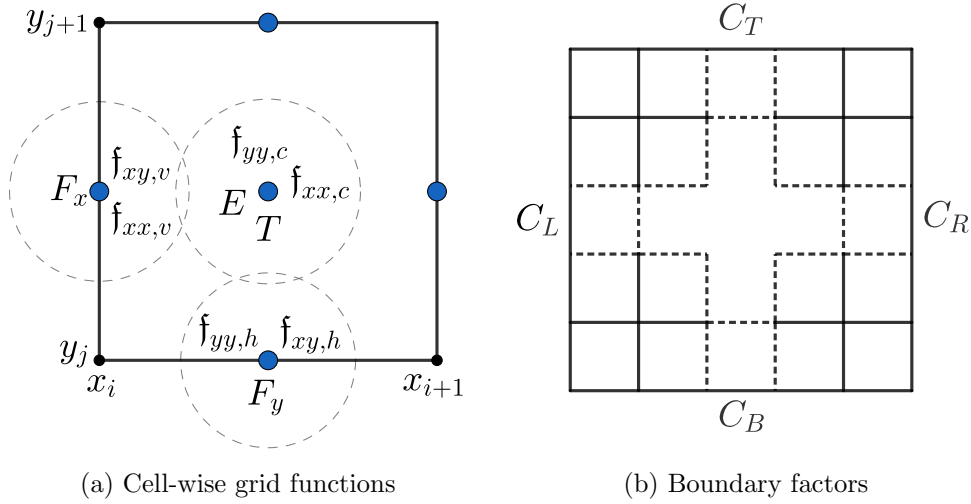
$$\boldsymbol{C}^n_{\theta,g} \in \mathbb{R}^{D_\theta}, \quad \theta = L, B, R, T \tag{36b}$$

with dimensions

$$D_L = D_R = Y, \quad D_B = D_T = X, \tag{37a}$$

$$D_v = (X+1)Y, \quad D_h = X(Y+1), \quad D_c = XY. \tag{37b}$$

Notations are illustrated in Figure 1.



(a) Cell-wise grid functions          (b) Boundary factors

Figure 1: Discrete grid functions shown on a sample 2D spatial mesh

The vectors in Eq. (36) are subsequently 'stacked' by frequency group to construct complete data vectors for each quantity at the $n^{\text{th}}$ time step

$$\mathbf{f}^n_{\alpha\beta,\gamma} = \left( (\mathfrak{f}^n_{\alpha\beta,1,\gamma})^\top \ (\mathfrak{f}^n_{\alpha\beta,2,\gamma})^\top \ \cdots \ (\mathfrak{f}^n_{\alpha\beta,G,\gamma})^\top \right)^\top \in \mathbb{R}^{GD_\gamma}, \tag{38a}$$

$$\boldsymbol{C}^n = \left( (\boldsymbol{C}^n_1)^\top \ (\boldsymbol{C}^n_2)^\top \ \cdots \ (\boldsymbol{C}^n_G)^\top \right)^\top \in \mathbb{R}^{2G(X+Y)}, \tag{38b}$$

where
$$\boldsymbol{C}^n_g = \left( (\boldsymbol{C}^n_{L,g})^\top \ (\boldsymbol{C}^n_{B,g})^\top \ (\boldsymbol{C}^n_{R,g})^\top \ (\boldsymbol{C}^n_{T,g})^\top \ \right)^\top \in \mathbb{R}^{2(X+Y)}. \tag{39}$$

Finally the vectors in Eq. (38) are collected in chronological order as columns of the following snapshot matrices

$$\mathbf{A}^{\mathfrak{f}_{\alpha\beta,\gamma}} = [\mathbf{f}^1_{\alpha\beta,\gamma} \ \mathbf{f}^2_{\alpha\beta,\gamma} \ \cdots \ \mathbf{f}^N_{\alpha\beta,\gamma}] \in \mathbb{R}^{GD_\gamma \times N}, \quad \mathbf{A}^c = [\boldsymbol{C}^1 \ \boldsymbol{C}^2 \ \cdots \ \boldsymbol{C}^N] \in \mathbb{R}^{2G(X+Y) \times N}, \tag{40}$$

where $N$ is the total number of time steps.

12

This process of data collection is repeated a sufficient number of times to sample a target parameter space with the FOM. Let $\mathbf{A}^{\mathfrak{f}_{\alpha\beta,\gamma}}(\vartheta)$, $\mathbf{A}^c(\vartheta)$ be the snapshot matrices that contain the solution to the TRT problem defined with a set of parameters $\vartheta \in \boldsymbol{\Theta}$, where $\boldsymbol{\Theta}$ is the space of problem parameters. The solutions to multiple realizations of the TRT problem, each defined with one of the parameter sets contained in $\{\vartheta_\ell\}_{\ell=1}^L \subset \boldsymbol{\Theta}$, are then held in the matrices $\mathbf{A}^{\mathfrak{f}_{\alpha\beta,\gamma}}(\vartheta_\ell)$, $\mathbf{A}^c(\vartheta_\ell)$. Each of these snapshot matrices is then projected onto some low-rank subspace as

$$\mathcal{A}_k^\phi(\vartheta_\ell) = \mathcal{G}_k \mathbf{A}^\phi(\vartheta_\ell), \quad k \leq \mathrm{rank}(\mathbf{A}^\phi(\vartheta_\ell)), \quad \phi = \mathfrak{f}_{\alpha\beta,\gamma}, \ C \tag{41}$$

where the projection operator $\mathcal{G}_k$ is defined by the specific method of data compression. The rank-$k$ representation of the matrix $\mathbf{A}^\phi$ of the form $\mathcal{A}_k^\phi \in \mathbb{C}^{D_A \times (k+\delta)}$ is constructed of $k$ sets of various vectors and factors (all of which may be complex), which in total comprise $D_A$ elements. Depending on the specific method used, $\delta$ can be 0 or 1. More concretely, $\mathcal{A}_k$ takes the following general form

$$\mathcal{A}_k \equiv \begin{cases} \bar{\boldsymbol{a}} \cup \{\boldsymbol{u}_i, \ \boldsymbol{v}_i, \ \sigma_i\}_{i=1}^k, & \text{POD} \\ \{\hat{\boldsymbol{\varphi}}_i, \ \omega_i, \ \beta_i\}_{i=1}^k, & \text{DMD} \\ \boldsymbol{a}_e \cup \{\hat{\boldsymbol{\varphi}}_i, \ \omega_i, \ \beta_i\}_{i=1}^k, & \text{DMD-E} \end{cases} \tag{42}$$

When grid functions of the Eddington tensor and boundary factors are to be calculated from $\{\mathcal{A}_k^{\mathfrak{f}_{\alpha\beta,\gamma}}(\vartheta_\ell)\}_{\ell=1}^L$ and $\{\mathcal{A}_k^c(\vartheta_\ell)\}_{\ell=1}^L$, the mapping operator $\mathcal{M}(t,\vartheta)$ is applied such that

$$\tilde{\boldsymbol{f}}_{\alpha\beta,\gamma}(t) = \mathcal{M}(t,\vartheta)\{\mathcal{A}_k^{\mathfrak{f}_{\alpha\beta,\gamma}}(\vartheta_\ell)\}_{\ell=1}^L. \tag{43}$$

Here $\tilde{\boldsymbol{f}}_{\alpha\beta,\gamma}(t) \in \mathbb{R}^{GD_\gamma}$ approximates the $\gamma$ grid function of the $\alpha\beta$ component of the Eddington tensor for the TRT problem with parameters $\vartheta$ at time $t$. The application of $\mathcal{M}(t,\vartheta)$ to $\{\mathcal{A}_k^c(\vartheta_\ell)\}_{\ell=1}^L$ similarly approximates the boundary factors for this TRT problem. $\mathcal{M}(t,\vartheta)$ consists of two separate operators

$$\mathcal{M}(t,\vartheta) = \mathcal{I}(\vartheta)\mathcal{H}(t), \tag{44}$$

where $\mathcal{H}(t)$ constructs a grid function at time $t$ from its low-rank representation and $\mathcal{I}(\vartheta)$ is an interpolation function of grid functions in $\boldsymbol{\Theta}$. If $t$ is one of the time instances used to generate the original snapshot matrices $\{\mathbf{A}(\vartheta_\ell)\}_{\ell=1}^L$, then $\mathcal{H}(t)\mathcal{A}_k$ simply regenerates that data. Otherwise $\mathcal{H}(t)$ constructs the grid functions nearest in time to $t$ and interpolates to $t$.

In essence, the obtained projections hold fundamental information on the Boltzmann transport solution (i.e. the radiation intensities). The Eddington tensor itself is a projection of the radiation intensities onto a low-dimensional subspace. That information is projected again onto a subspace of even lower dimensionality using the POD and DMD. This holds several benefits. The computational burden of computing the LOQD closures is lessened as we can store the needed high-order data efficiently in memory, and fewer computations are required to interpolate between this data. The rank $k$ of approximation is easily modified

---

**Algorithm 2:** Obtaining the solution to TRT problems with the DET class of ROMs

---

Input: $\{\mathcal{A}_k^{\mathfrak{f}}(\vartheta_\ell)\}_{\ell=1}^L$, $\{\mathcal{A}_k^c(\vartheta_\ell)\}_{\ell=1}^L$, $\mathcal{M}$

$n = 0$

**while** $t_n \leq t^{end}$ **do**

    $n = n + 1$

    Compute $\tilde{\mathbf{f}}_g = \mathcal{M}(t^n, \vartheta)\{\mathcal{A}_k^{\mathfrak{f}}(\vartheta_\ell)\}_{\ell=1}^L$

    Compute $\tilde{C}_g = \mathcal{M}(t^n, \vartheta)\{\mathcal{A}_k^c(\vartheta_\ell)\}_{\ell=1}^L$

    $T^{(0)} = T^{n-1}$

    $q = 0$

    **while** $\|T^{(q)} - T^{(q-1)}\| > \epsilon_1 \|T^{(q)}\| + \epsilon_2, \quad \|E^{(q)} - E^{(q-1)}\| > \epsilon_1 \|E^{(q)}\| + \epsilon_2$ **do**

        Update $B_g, \varkappa_g$ with $T^{(q)}$

        Solve multigroup LOQD equations (8) with $\tilde{\mathbf{f}}_g$ & $\tilde{C}_g$ for $E_g^{(q)}$, $\boldsymbol{F}_g^{(q)}$

        Compute spectrum-averaged coefficients in Eq. (14)

        Solve effective grey problem (13) & (17) for $T^{(q+1)}$, $E^{(q+1)}$, $\boldsymbol{F}^{(q+1)}$

        $q = q + 1$

    **end**

    $T^n \leftarrow T^{(q)}$

**end**

---

to accommodate different simulations, allowing one to adjust the approximation errors and computational load.

The method for solving TRT problems with the DET ROMs is summarized in Algorithm 2. At each $n^{\text{th}}$ time step, the corresponding grid functions of the Eddington tensor and boundary factors are generated by applying the operator $\mathcal{M}(t^n)$ to the input compressed data $\mathcal{A}_k$. Then the material temperature and total radiation energy density are calculated iteratively. At each $q$ iteration the compressed representations of the Eddington tensor and boundary factor data are used to define the multigroup LOQD equations. The solution to the multigroup LOQD equations is used to generate all effective grey opacities and factors. The effective grey problem formed by the coupled effective grey LOQD and MEB equations is subsequently solved via Newton's method to obtain the material temperature, total radiation energy density and total radiation flux.

## 6. Accuracy and Convergence of DET ROMs versus Rank of Eddington Tensor Approximation

### 6.1. Reduced-Order Model Analysis

A general purpose of ROMs is to find solutions of problems that have yet to be solved (i.e. for $\vartheta \notin \{\vartheta_\ell\}_{\ell=1}^L$). Before such an application can be considered however, certain

qualities of the ROM must be identified. It is imperative to demonstrate how well the ROM can reconstruct a known FOM solution. The essential question concerns convergence behavior of $E$ and $T$ with decrease of $\xi$ and hence with increase in rank of approximation of the Eddington tensor. Accuracy of ROM TRT solutions in time (and phase space) with different values of $\xi$ is another research item. Such analysis will enable one to determine how the ROM can achieve a desired level of accuracy and reproduce essential characteristics of physical phenomena and physical effects.

Numerical tests are performed on the models to investigate their properties and performance. This numerical testing is done in two stages to investigate the ROM's performance. First the non-parametric case is explored, followed by the parametric case. In the non-parametric case, a 'base-case' or reference FOM solution is found for some test problem to form the ROM database, and then the same test problem is solved again with the ROM. Comparisons of the ROM solution to the known FOM solution can be carried out on the considered discrete grids in phase space and time. It is important to note that the only errors incurred by our FOM are due to discretization and as such the FOM will converge to the continuous TRT solution in the limit with refinement of grids in phase space and time.

In the non-parametric case, numerical results will be shown with the objective of identifying (i) how accurate the ROM solutions are relative to the FOM solution, (ii) whether the ROM solutions converge to the FOM solution as $\xi$ decreases towards zero, and (iii) if the ROM solutions do converge to the FOM solution, whether they do so in a well-behaved manner.

## 6.2. Test Problem

To analyze the accuracy of the DET ROMs, we use a 2-dimensional extension of the well-known Fleck-Cummings (F-C) test problem [98]. This F-C test takes the form of a square homogeneous domain in the $x-y$ plane, 6 cm in length on both sides. The domain is initially at a temperature of $T^0$, the left boundary of the domain is subject to incoming radiation with blackbody spectrum at a temperature of $T^{\text{in}}$, and there is no incoming radiation at other boundaries. The selected reference parameters to be used here are $T^0 = 1$ eV and $T^{\text{in}} = 1$ KeV. The material is characterized by an opacity of

$$\varkappa_\nu = \frac{27}{\nu^3}\left(1 - e^{-\frac{\nu}{T}}\right), \tag{45}$$

and a material energy density that is linear in temperature

$$\varepsilon(T) = c_v T, \tag{46}$$

with material heat capacity $c_v = 0.5917 a_R (T^{\text{in}})^3$. The time interval of the problem is [0,6 ns].

All equations are discretized in time with the implicit backward-Euler integration scheme. The BTE is discretized in phase space with the discrete ordinates and simple corner balance schemes [106]. All low-order moment equations are discretized with a 2$^{\text{nd}}$-order finite volumes scheme in space [105]. A uniform grid of $20 \times 20$ cells (i.e. $X = Y = 20$) with side lengths of $\Delta x = \Delta y = 0.3$ cm is used to discretize the slab. $G = 17$ frequency groups are defined as shown in Table 1. The Abu-Shumays angular quadrature set q461214 with 36 discrete

Table 1: Upper boundaries for each frequency group

| $g$ | 1 | 2 | 3 | 4 | 5 | 6 | 7 | 8 | 9 |
|---|---|---|---|---|---|---|---|---|---|
| $\nu_g$ [KeV] | 0.7075 | 1.415 | 2.123 | 2.830 | 3.538 | 4.245 | 5.129 | 6.014 | 6.898 |
| $g$ | 10 | 11 | 12 | 13 | 14 | 15 | 16 | 17 | |
| $\nu_g$ [KeV] | 7.783 | 8.667 | 9.551 | 10.44 | 11.32 | 12.20 | 13.09 | $1\times10^7$ | |
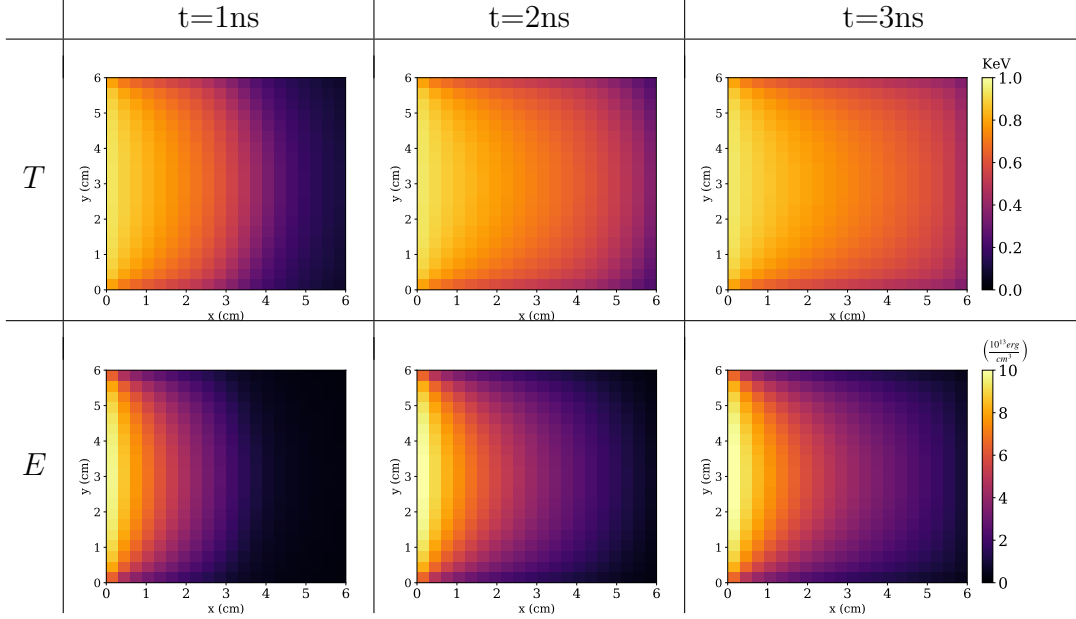


Figure 2: F-C test solution for the material temperature ($T$) and total radiation energy density ($E$) over the spatial domain at times t=1, 2, 3 ns.

directions per quadrant is used [107]. The total number of angular directions is $M = 144$. The F-C problem is solved for the specified time interval $t \in [0,6 \text{ ns}]$ with $N = 300$ uniform time steps $\Delta t = 2 \times 10^{-2}$ ns. When generating ROM solutions to the F-C problem, the following convergence criteria are used (ref. Algorithm 2): $\epsilon_1 = 10^{-14}$ and $\epsilon_2 = 10^{-15}$.

The solution to this F-C test for the material temperature and total radiation energy density at times $t = 1, 2, 3$ ns is depicted in Figure 2. The solutions of both $T$ and $E$ take the form of a wave that first rapidly forms on the left boundary before propagating to the right. After this the domain is continuously heated. Eventually the solution reaches a regime close to steady state.

The total number of DoF occupied by the Eddington tensor $\mathfrak{f}_g$ at a single instant of time is $D_\mathfrak{f} = 2(D_v + D_h + D_c)G = 4.216 \times 10^4$. In comparison, the DoF occupied by the radiation intensities from the simple corner balance scheme equals $D_I = 4XYMG = 3.9168 \times 10^6$. This means that even before compressing the Eddington tensor with the POD or DMD, the required memory occupation is $\frac{D_I}{D_\mathfrak{f}} = 93$ times smaller than for the radiation intensities.
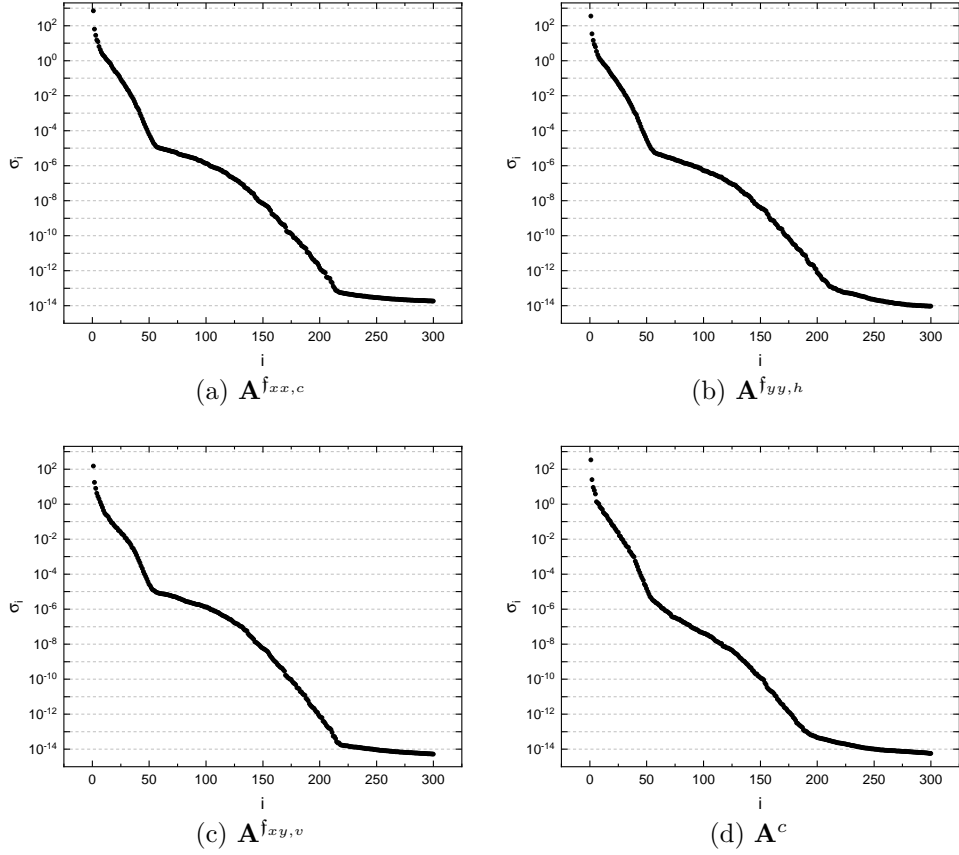
Figure 3: Singular value distributions of select snapshot matrices of grid functions of the Eddington tensor and boundary factor for the F-C test. $i$ is the singular value index. The included matrices are: (a) $\mathbf{A}^{\mathfrak{f}xx,c}$, (b) $\mathbf{A}^{\mathfrak{f}yy,h}$, (c) $\mathbf{A}^{\mathfrak{f}xy,v}$, (d) $\mathbf{A}^c$.

## 6.3. Data Analysis

The snapshot data used to construct the matrices $\mathbf{A}^{\mathfrak{f}\alpha\beta,\gamma}$ and $\mathbf{A}^c$ (see Eq. (40)) is obtained by solving the TRT problem (Eqs. (1) & (4)) on the given grid in phase-space and time by means of the MLQD method. This is the FOM solution of the test problem that is used as the reference solution. The singular values of a select few of these snapshot matrices are depicted in Figure 3. The singular values of those databases not shown here do not deviate significantly from the chosen plots. The singular values for each of the databases decay in a similar manner with 3 distinct sharp drops in magnitudes before reaching a value of approximately $10^{-14}$ where decay halts. The singular values that have a value at or below $10^{-14}$ have reached the limit of machine precision and can be considered numerically zero.

Although the POD, DMD and DMD-E make use of slight variations on these snapshot matrices, the singular value distributions of these variant matrices are very similar to those pictured. For the databases without their final column, used for the DMD, their SVD is almost exactly the same as for the full matrices since the final column holds near steady-state data and does not add much new information to the span of the columns. For the POD

17

Table 2: Ranks $k$ for each approximate database corresponding to different values of $\xi$ for the POD

| $\xi$ | $\mathcal{A}^{\mathfrak{f}_{xx,c}}$ | $\mathcal{A}^{\mathfrak{f}_{xx,v}}$ | $\mathcal{A}^{\mathfrak{f}_{yy,c}}$ | $\mathcal{A}^{\mathfrak{f}_{yy,h}}$ | $\mathcal{A}^{\mathfrak{f}_{xy,v}}$ | $\mathcal{A}^{\mathfrak{f}_{xy,h}}$ | $\mathcal{A}^{c}$ |
|---|---|---|---|---|---|---|---|
| $10^{-2}$ | 15 | 17 | 15 | 15 | 14 | 17 | 14 |
| $10^{-4}$ | 34 | 36 | 34 | 34 | 37 | 36 | 35 |
| $10^{-6}$ | 49 | 49 | 52 | 49 | 65 | 68 | 48 |
| $10^{-8}$ | 115 | 110 | 120 | 115 | 129 | 127 | 87 |
| $10^{-10}$ | 152 | 148 | 154 | 153 | 159 | 158 | 132 |
| $10^{-12}$ | 179 | 178 | 180 | 180 | 185 | 184 | 160 |
| $10^{-14}$ | 203 | 203 | 205 | 205 | 207 | 207 | 188 |
| $10^{-16}$ | 300 | 300 | 300 | 300 | 300 | 300 | 300 |
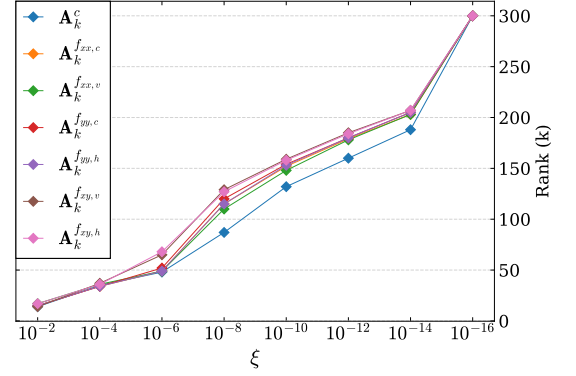


Figure 4: Plotted ranks $k$ for the POD (see Table 2)

Table 3: Ranks $k$ for each approximate database corresponding to different values of $\xi$ for the DMD

| $\xi$ | $\mathcal{A}^{\mathfrak{f}_{xx,c}}$ | $\mathcal{A}^{\mathfrak{f}_{xx,v}}$ | $\mathcal{A}^{\mathfrak{f}_{yy,c}}$ | $\mathcal{A}^{\mathfrak{f}_{yy,h}}$ | $\mathcal{A}^{\mathfrak{f}_{xy,v}}$ | $\mathcal{A}^{\mathfrak{f}_{xy,h}}$ | $\mathcal{A}^{c}$ |
|---|---|---|---|---|---|---|---|
| $10^{-2}$ | 6 | 7 | 6 | 6 | 7 | 9 | 5 |
| $10^{-4}$ | 28 | 30 | 28 | 28 | 30 | 30 | 25 |
| $10^{-6}$ | 43 | 44 | 44 | 43 | 46 | 46 | 42 |
| $10^{-8}$ | 90 | 79 | 100 | 87 | 111 | 111 | 61 |
| $10^{-10}$ | 138 | 136 | 142 | 139 | 148 | 147 | 112 |
| $10^{-12}$ | 168 | 165 | 170 | 169 | 175 | 175 | 147 |
| $10^{-14}$ | 195 | 194 | 196 | 196 | 199 | 199 | 173 |
| $10^{-16}$ | 286 | 286 | 287 | 287 | 292 | 291 | 274 |
| $10^{-18}$ | 299 | 299 | 299 | 299 | 299 | 299 | 299 |
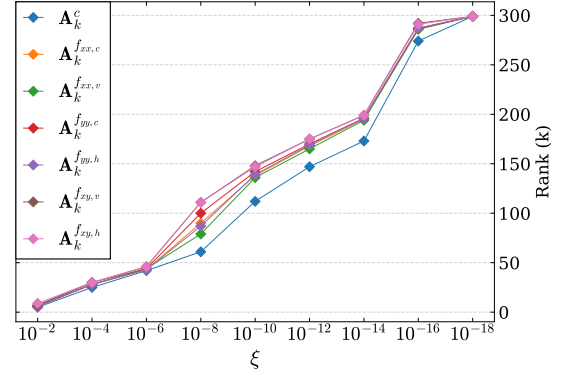


Figure 5: Plotted ranks $k$ for the DMD (see Table 3)

Table 4: Ranks $k$ for each approximate database corresponding to different values of $\xi$ for the DMD-E

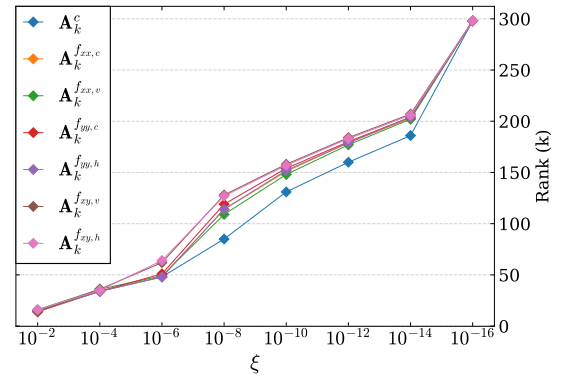| $\xi$ | $\mathcal{A}^{\mathfrak{f}_{xx,c}}$ | $\mathcal{A}^{\mathfrak{f}_{xx,v}}$ | $\mathcal{A}^{\mathfrak{f}_{yy,c}}$ | $\mathcal{A}^{\mathfrak{f}_{yy,h}}$ | $\mathcal{A}^{\mathfrak{f}_{xy,v}}$ | $\mathcal{A}^{\mathfrak{f}_{xy,h}}$ | $\mathcal{A}^{c}$ |
|---|---|---|---|---|---|---|---|
| $10^{-2}$ | 14 | 16 | 15 | 15 | 14 | 16 | 14 |
| $10^{-4}$ | 34 | 36 | 34 | 34 | 36 | 35 | 34 |
| $10^{-6}$ | 48 | 49 | 51 | 48 | 62 | 64 | 48 |
| $10^{-8}$ | 114 | 109 | 119 | 114 | 125 | 127 | 85 |
| $10^{-10}$ | 151 | 148 | 154 | 152 | 158 | 157 | 131 |
| $10^{-12}$ | 179 | 177 | 180 | 179 | 184 | 183 | 160 |
| $10^{-14}$ | 203 | 202 | 204 | 204 | 207 | 206 | 186 |
| $10^{-16}$ | 298 | 298 | 298 | 298 | 298 | 298 | 298 |



Figure 6: Plotted ranks $k$ for the DMD-E (see Table 4)

when the databases are centered about their column-mean, the only significant difference from the shown plots is in the first singular value which decreases by roughly an order of magnitude. The second singular value is also seen to decrease by roughly half. The equilibrium-subtracted databases used for the DMD-E acquire singular value spectra very similar to those obtained through the POD.

The POD, DMD and DMD-E are applied to the databases $\mathbf{A}^{\mathfrak{f}\alpha\beta,\gamma}$ and $\mathbf{A}^c$ to generate several different rank-$k$ approximations of the FOM Eddington tensor data. For each method of approximation, several ranks $k$ were determined to satisfy a spectrum of chosen values for $\xi$ while calculating the TSVD (Eq. (26)). Tables 2, 3 and 4 display the ranks used to approximate each individual database for every $\xi$. Figures 4, 5 and 6 plot these ranks against $\xi$. The ranks used for the POD, DMD and DMD-E behave similarly with changes in $\xi$ for each snapshot matrix, gradually increasing with decreases in $\xi$ until $\xi = 10^{-16}$ where each database's rank increases by roughly 100. This is due to the singular value decay structures shown in Figure 3 where decay stops after about 200 singular values. The only significant difference in the used ranks between each of these methods given the same $\xi$ is that the DMD always uses a lower rank than the POD and DMD-E. This is an artifact of the centering and equilibrium-subtraction operations done on the databases prior to the calculation of each TSVD for the POD and DMD-E. Here these operations only significantly decreased the first and second singular values of each matrix. This has the effect of reducing only the denominator of Eq. (25) for all $k > 1$ and therefore inflating the rank required to satisfy a given $\xi$.

### 6.4. Analysis of ROM Solution Errors

We now analyze the solutions of the F-C test computed by DET ROMs with the reduced-rank databases $\mathcal{A}_k^{\mathfrak{f}\alpha\beta,\gamma}$ and $\mathcal{A}_k^c$. Figures 7, 8 and 9 show the relative error for the material temperature ($T$) and total radiation energy density ($E$) calculated in the 2-norm over space at each instant of time in $t \in [0, 6\text{ns}]$ where each unique curve corresponds to the ROM solution generated for a given value of $\xi$. Note that errors are calculated relative to the reference FOM solution used to generate $\mathcal{A}_k^{\mathfrak{f}\alpha\beta,\gamma}$ and $\mathcal{A}_k^c$.

Considering first the ROM using the POD, Figure 7 demonstrates a uniform convergence of errors in time as $\xi$ is decreased. The error curves all behave similarly in time as well, first increasing in the rapidly evolving physical regime of wave evolution followed by stabilization to the neighborhood of some value for times after roughly 0.5ns. The highest observed errors are on the order of $10^{-4}$, corresponding to the ROM with $\xi = 10^{-2}$. When $\xi = 10^{-16}$, the POD ROM invokes a full-rank representation of the Eddington tensor data and finds errors on the order of $10^{-15}$, successfully obtaining the FOM solution to numerical precision. Next looking at the ROM using the DMD, Figure 8 shows uniform convergence of the ROM errors in time for $\xi$ decreasing until $\xi = 10^{-12}$. Further decreases in $\xi$ have the effect of decreasing errors while $t > 2.5$ns and increasing errors for $t < 2.5$ns. The lowest errors for a single value of $\xi$ exist on the order of $10^{-12} - 10^{-10}$. These effects are attributed to numerical noise, of which the DMD has known susceptibility to [28, 103]. Results for $\xi = 10^{-18}$ are not shown here as there is no significant change from those seen for $\xi = 10^{-16}$. The highest errors observed with the DMD are on the order of $10^{-2}$ for $\xi = 10^{-2}$, 2 orders of magnitude

higher than observed for the POD with the same $\xi$. Lastly, the ROM using the DMD-E suffers from an amplified sensitivity to numerical noise in calculations with high-rank approximations compared to the ROM with the DMD. Errors shown in Figure 9 are seen to converge up until $\xi = 10^{-10}$, after which further decreases in $\xi$ lead to increases in the ROM errors. This effect is primarily observed for the early time instances of the problem. In contrast, the later times tend to stagnate at the same level of error as $\xi$ decreases.



(a) Material Temperature

(b) Radiation Energy Density
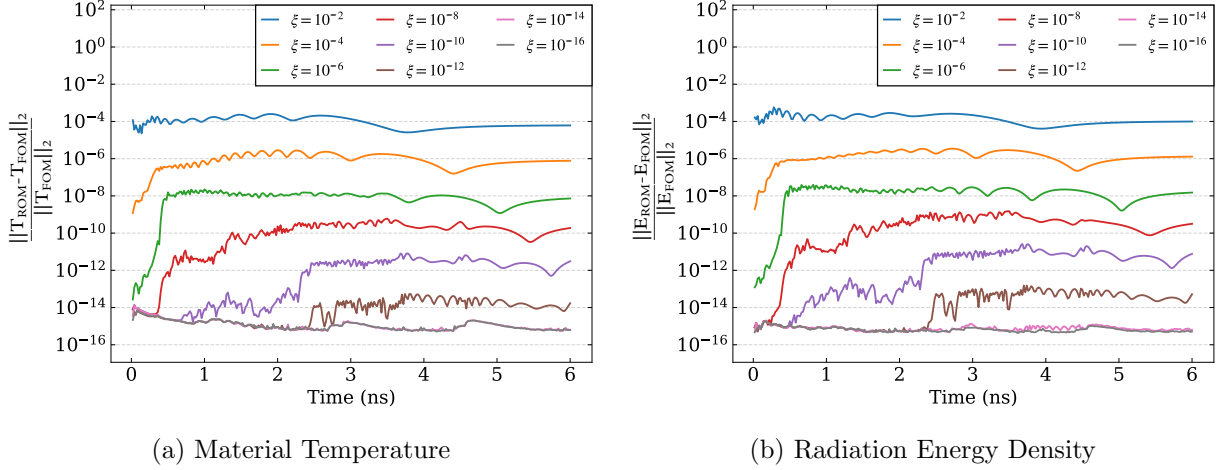
Figure 7: Relative errors in the 2-norm of the DET ROM using the POD using several $\xi$, plotted vs time



(a) Material Temperature

(b) Radiation Energy Density
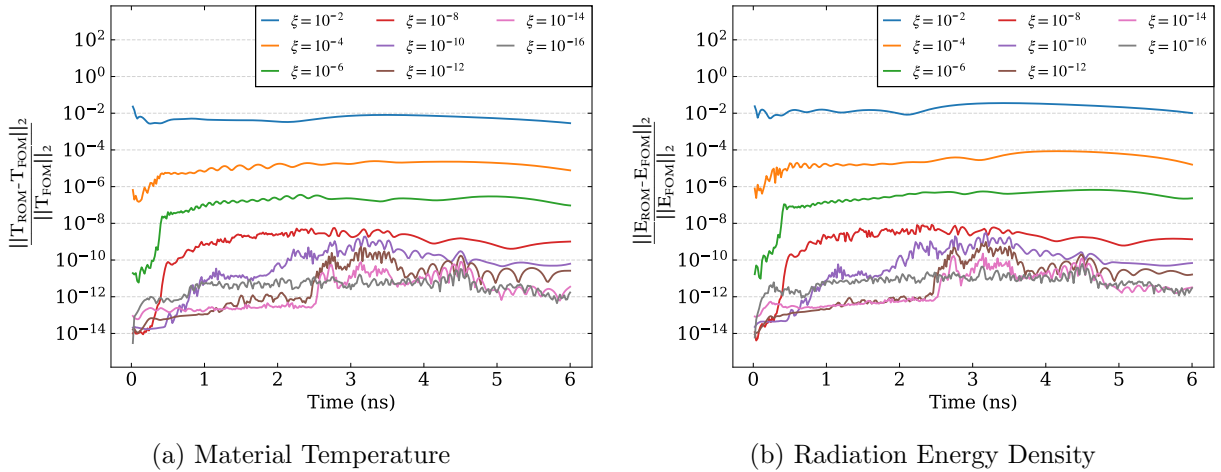
Figure 8: Relative errors in the 2-norm of the DET ROM using the DMD using several $\xi$, plotted vs time

A different view of the data presented in Figures 7 - 9 is given in Figures 10, 11 and 12. These plots graph the ROM errors (w.r.t. the FOM solution) in the relative 2-norm against $\xi$, with each curve corresponding to a specific instant in time. These plots show convergence behavior of DET ROMs at various instances. Let the errors of each ROM be written as the function $\epsilon(x) = \frac{\|x_{\text{FOM}} - x_{\text{ROM}}\|_2}{\|x_{\text{FOM}}\|_2}$. From Figure 10, it is immediately evident that the errors associated with the POD ROM have the relationship $\epsilon(E) \approx \epsilon(T) \approx \xi \cdot 10^{-2}$ up to the point

20

where stagnation occurs from limitations of the finite precision of calculations. Figure 11 shows a similar relationship for the DMD ROM, with $\epsilon(E) \approx \epsilon(T) \approx \xi$ for $\xi \geq 10^{-8}$. A decrease in the rate of convergence is observed for $\xi < 10^{-8}$ with this ROM before stagnation occurs around an order of $10^{-12} - 10^{-10}$. This slow in convergence rate is attributed again to an increase in numerical noise as rank is increased.
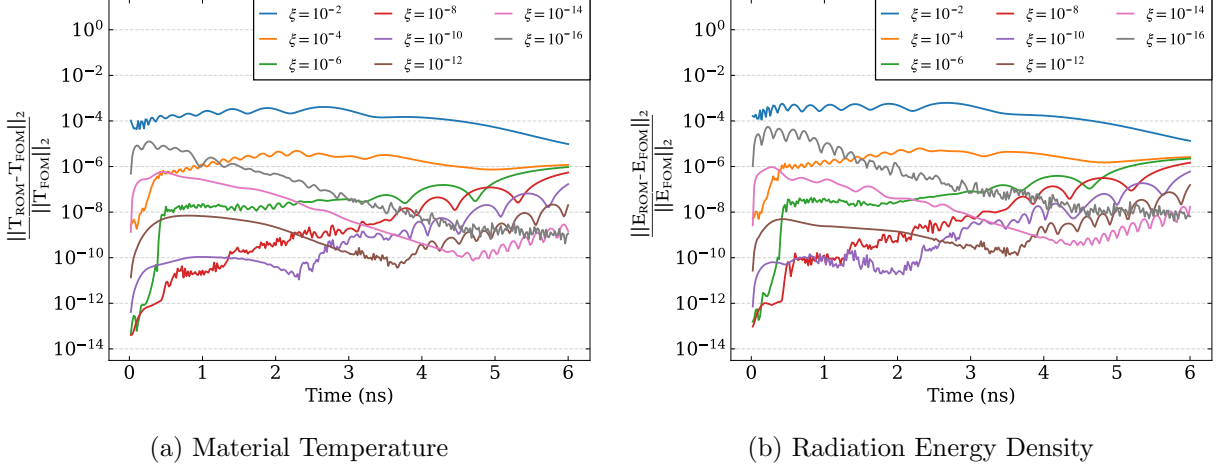


| (a) Material Temperature | (b) Radiation Energy Density |

Figure 9: Relative errors in the 2-norm of the DET ROM using the DMD-E using several $\xi$, plotted vs time



| (a) Material Temperature | (b) Radiation Energy Density |
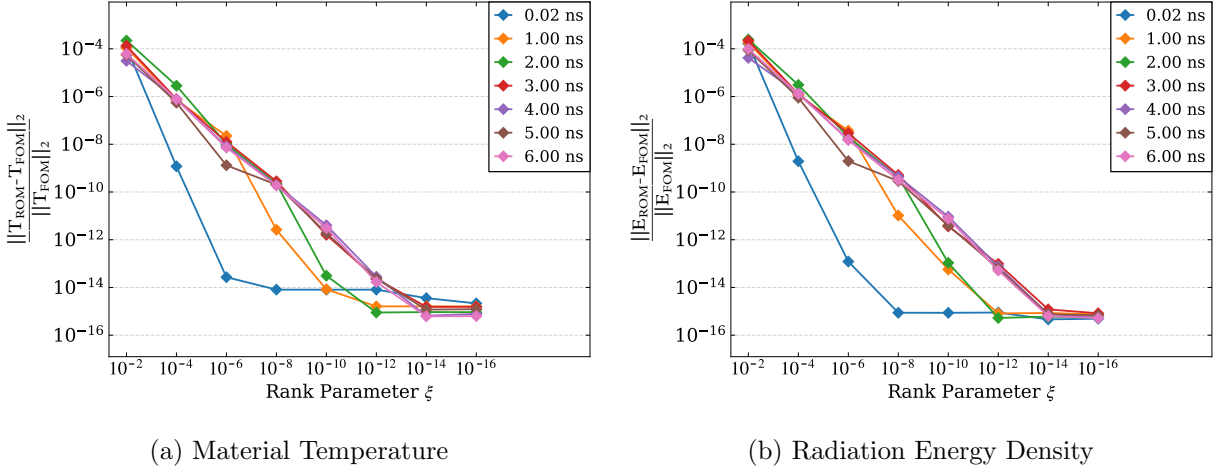
Figure 10: Relative errors in the 2-norm of the DET ROM using the POD at several times, plotted vs $\xi$

Lastly considering the DMD-E ROM, Figure 12 demonstrates the observed sensitivity to numerical noise for small $\xi$. An initial increase in error level is seen at times $t = .02, 1$ ns for $\xi = 10^{-10}$, and the errors at $t = 2$ ns increase at $\xi = 10^{-12}$. This behavior is accredited to a large magnification of numerical errors as seen with the DMD. The DMD-E can be interpreted as the DMD on a set of residual vectors representing the distance of the expanded data to the near steady-state solution. The residual vectors for near steady-state data are then expected to have elements of very small magnitude which can contribute

to numerical issues in the decomposition. This combined with the inherent sensitivity of the DMD to numerics can lead to large amplifications of error. This interpretation also gives justification to the behaviors seen in Figure 9. The exponentials in Eq. (34) are expected to decrease toward zero as time moves onward so that the 'steady-state' solution is only represented by the constant term. Any amount of noise introduced into the DMD-E expansion will become less prevalent as $t$ grows and the exponentials shrink.
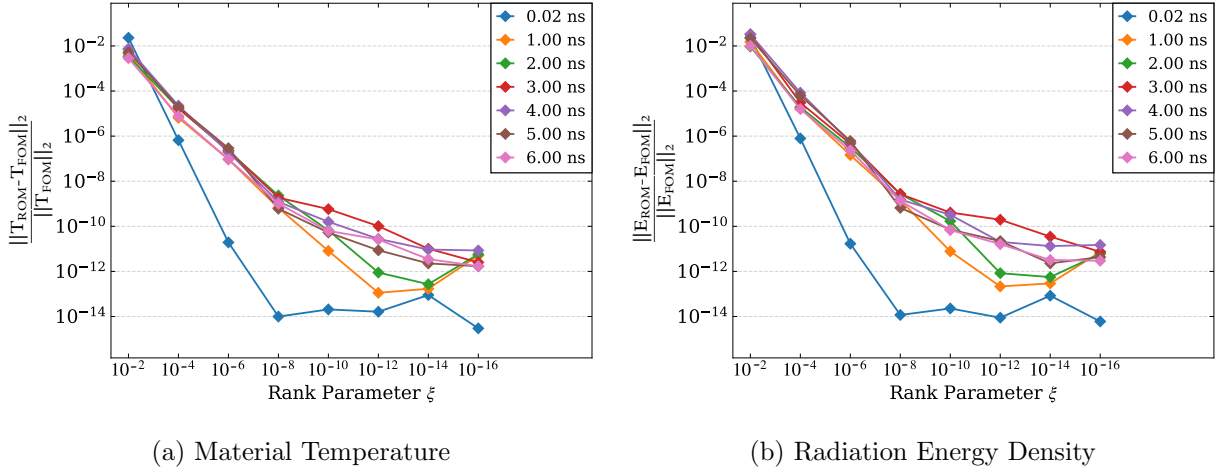


(a) Material Temperature

(b) Radiation Energy Density

Figure 11: Relative errors in the 2-norm of the DET ROM using the DMD at several times, plotted vs $\xi$



(a) Material Temperature

(b) Radiation Energy Density
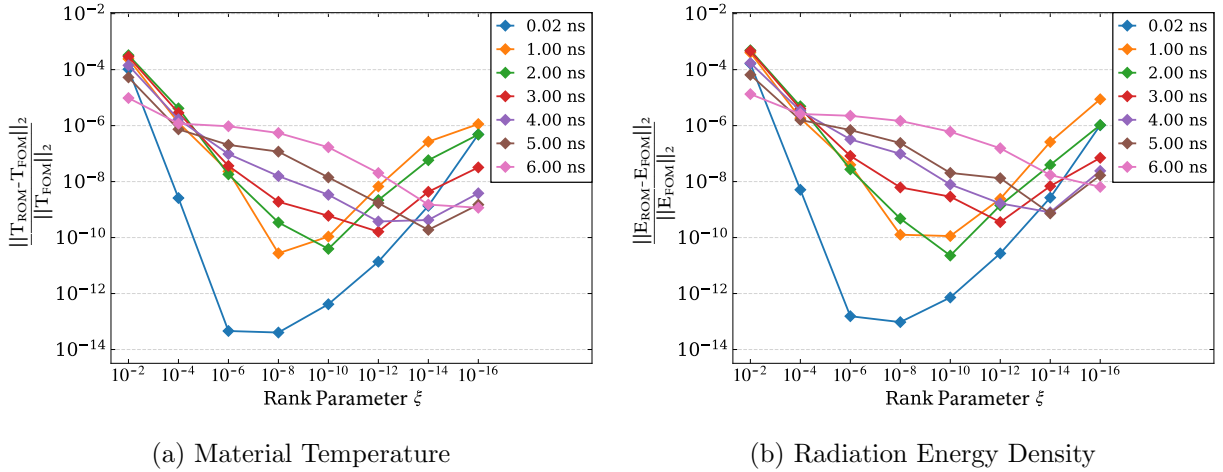
Figure 12: Relative errors in the 2-norm of the DET ROM using the DMD-E at several times, plotted vs $\xi$

The results presented up this point indicate that when equipped with methods like the POD and DMD, the DET class of ROMs can successfully and predictably converge to the FOM solutions they were trained on. This property is not exhibited with use of the DMD-E. Even so, in every case the DET ROMs are shown to perform well with low-rank. In practice, it is the low-rank ROMs which are the most important as undoubtedly the DET ROM reaps

the most computational benefits with larger $\xi$ (i.e. $\xi = 10^{-2}, 10^{-4}$).

The analysis thus far has studied ROM errors in 2-norm over space. The local behavior of errors over the spatial domain is now considered for the DET ROMs with $\xi = 10^{-2}, 10^{-4}$. Figures 13, 14 and 15 show cell-wise relative errors in $T$ and $E$ at selected instants of time. Each of these figures takes the form of two tables that display the relative pointwise error in the DET ROM across the spatial domain of the F-C test. The first (top) table shows errors in the material temperature ($T$) and the second (bottom) shows errors in the total radiation energy density ($E$). Each row corresponds to a different value of $\xi$ and each column corresponds to the specific instant of time. These include $\xi = 10^{-2}, 10^{-4}$ and $t = 1, 2, 3$ ns, respectively. All plots contained on a single row use the same scale for their color distributions. In order, Figures 13, 14 and 15 correspond to the errors in the DET ROMs equipped with the POD, DMD and DMD-E. These figures demonstrate that the spatial distribution of errors in those low-rank ROMs is relatively uniform. There are no sharp changes in the error about spatial position and each point has an error value residing in a close neighborhood to the relative 2-norm error for the corresponding ROM and time point shown in Figures 7, 8 and 9. Further analysis has shown similar results for higher rank DET ROMs.

### 6.5. Analysis of Radiation Wave Propagation

We now consider properties of the DET class of ROMs in capturing certain physics of TRT problems. One metric of particular importance is *breakout time* of radiation that characterises how well the ROMs are able to reproduce the FOM radiation wavefront as it propagates through the spatial domain [81, 83]. The radiation wave produced in the F-C test travels from left to right and correspondingly the notion of breakout time is associated with radiation levels at the right boundary. Typically in the literature, breakout time is measured as the elapsed time until a certain level of radiative flux is detected [81, 83]. Here we consider not only the radiation flux, but the energy density and material temperature at the right boundary of the F-C test as well. We consider the boundary-averages of these quantities, defined as follows:

$$\bar{F}_R = \frac{1}{L_R} \int_0^{L_R} \boldsymbol{e}_x \cdot \boldsymbol{F}(x_R, y) \ dy, \tag{47a}$$

$$\bar{E}_R = \frac{1}{L_R} \int_0^{L_R} E(x_R, y) \ dy, \tag{47b}$$

$$\bar{T}_R = \frac{1}{L_R} \int_0^{L_R} T(x_R, y) \ dy, \tag{47c}$$

where $L_R = x_R = 6$cm. The time evolution of $\bar{F}_R$, $\bar{E}_R$, and $\bar{T}_R$, calculated with the FOM is depicted in Figure 16. These figures show two sharp increases in $\bar{F}_R$ and $\bar{E}_R$ followed by plateaus, whereas $\bar{T}_R$ increases smoothly until reaching a final plateau. The initial plateaus for $\bar{F}_R$, $\bar{E}_R$ occur at roughly 0.5 ns and indicate when the high-energy radiation has penetrated the domain. The final plateaus for each $\bar{F}_R$, $\bar{E}_R$, and $\bar{T}_R$ occurs at about 2.5 ns, indicating full penetration of the domain.
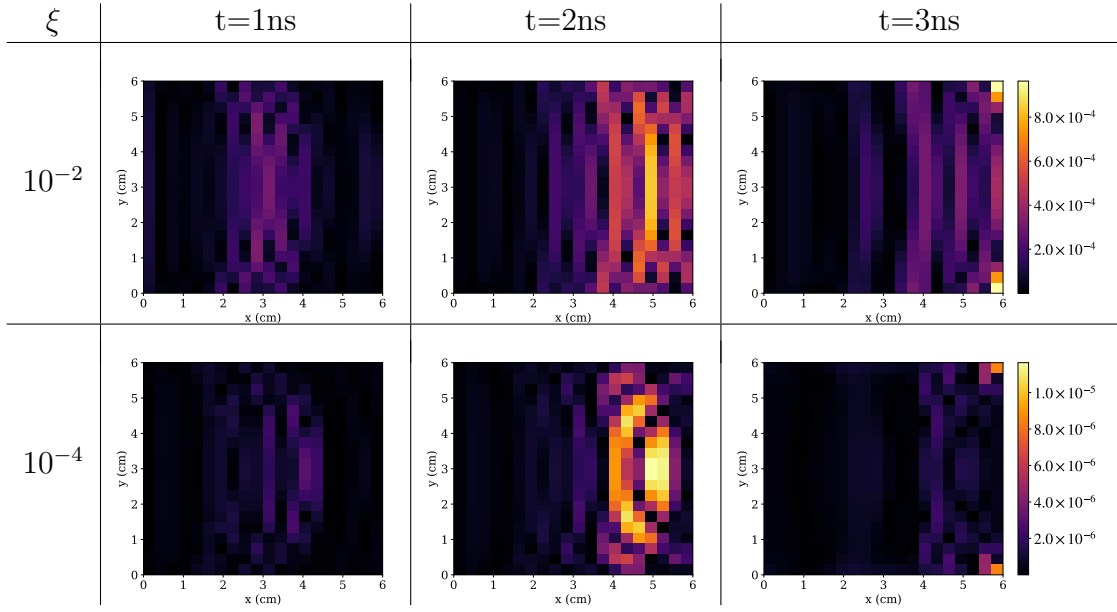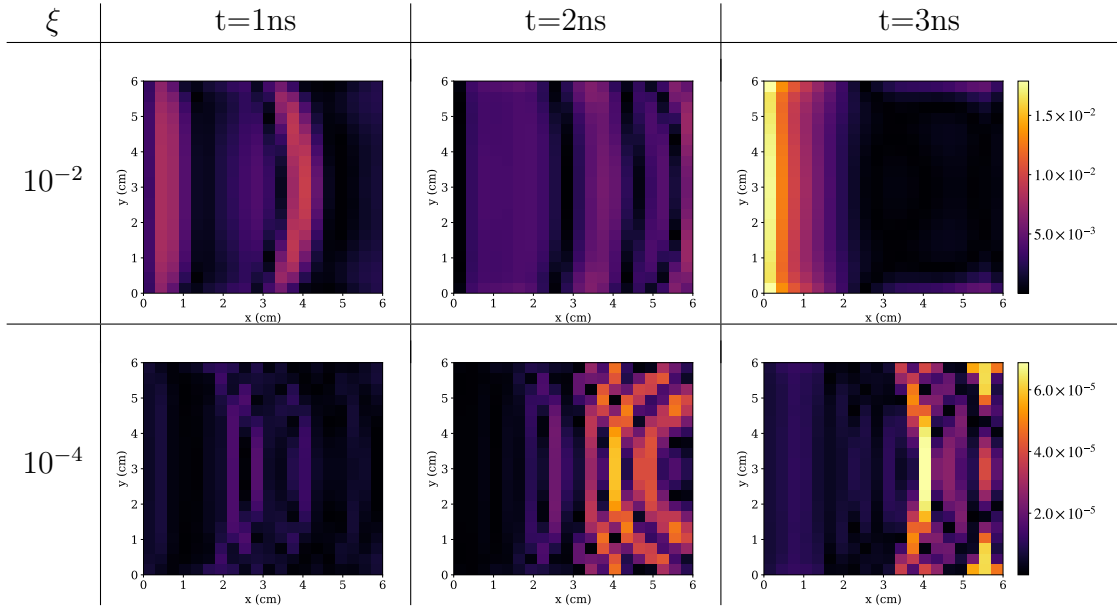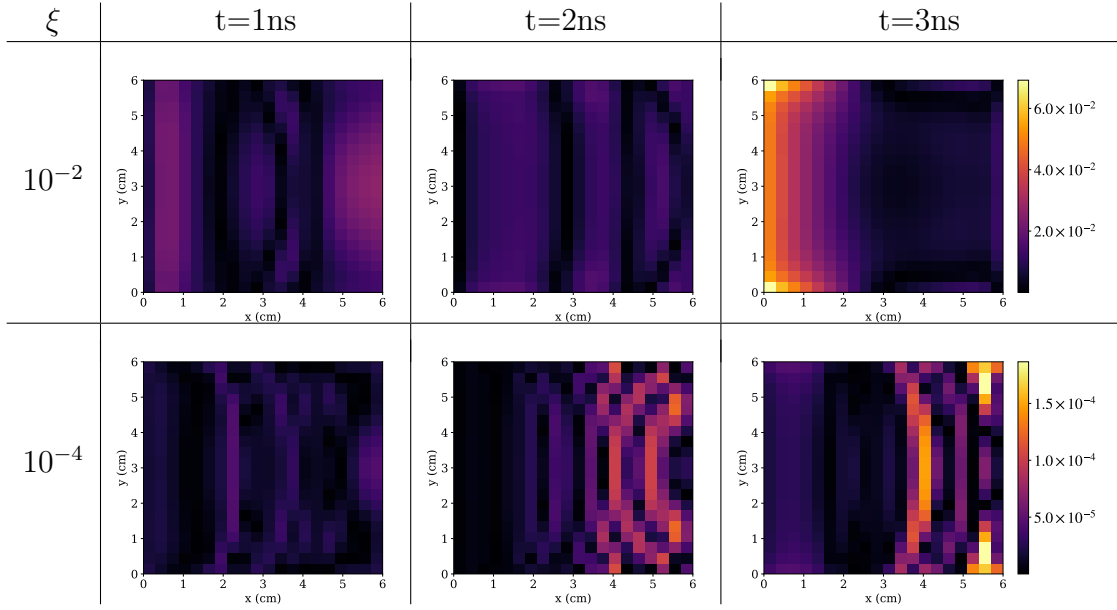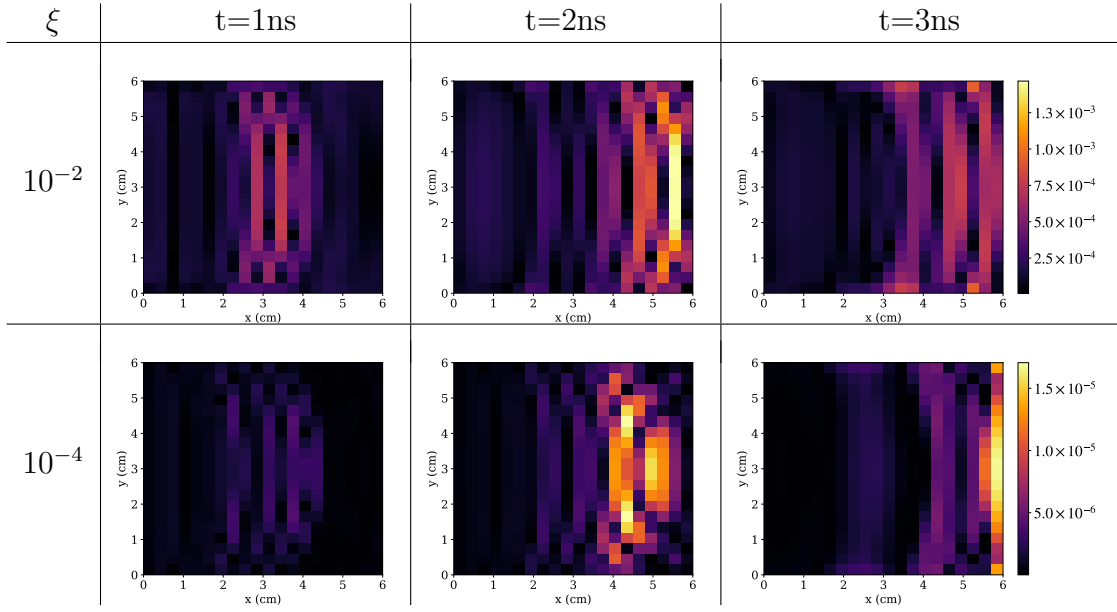
(a) Material Temperature
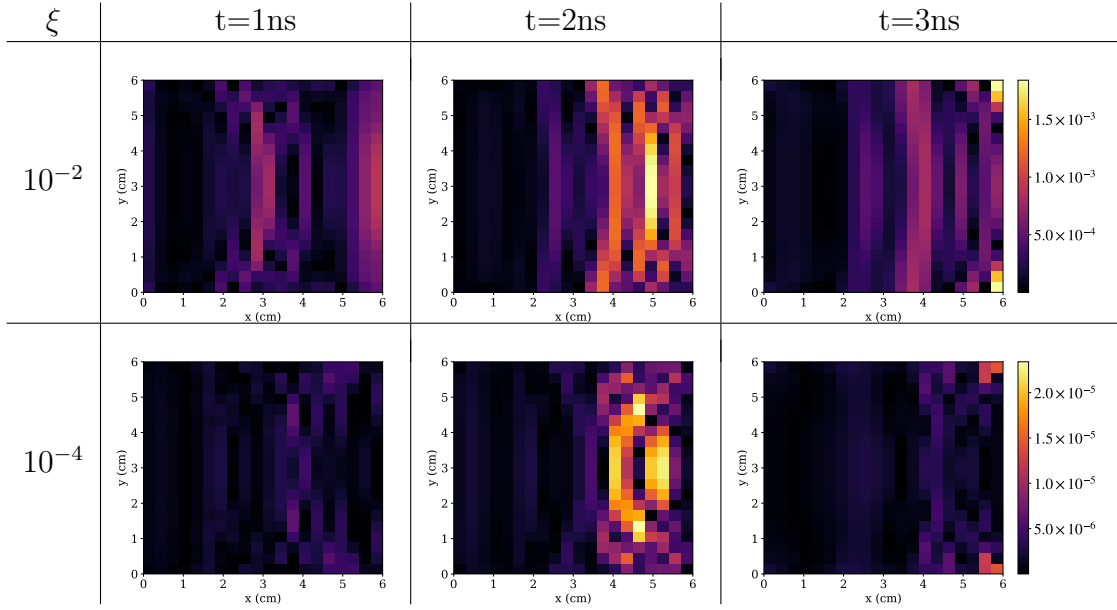


(b) Radiation Energy Density

Figure 13: Cell-wise relative error in material temperature ($T$) and total radiation energy density ($E$) over the spatial domain at times t=1, 2, 3 ns for the DET ROM equipped with the POD for $\xi = 10^{-2}, 10^{-4}$.
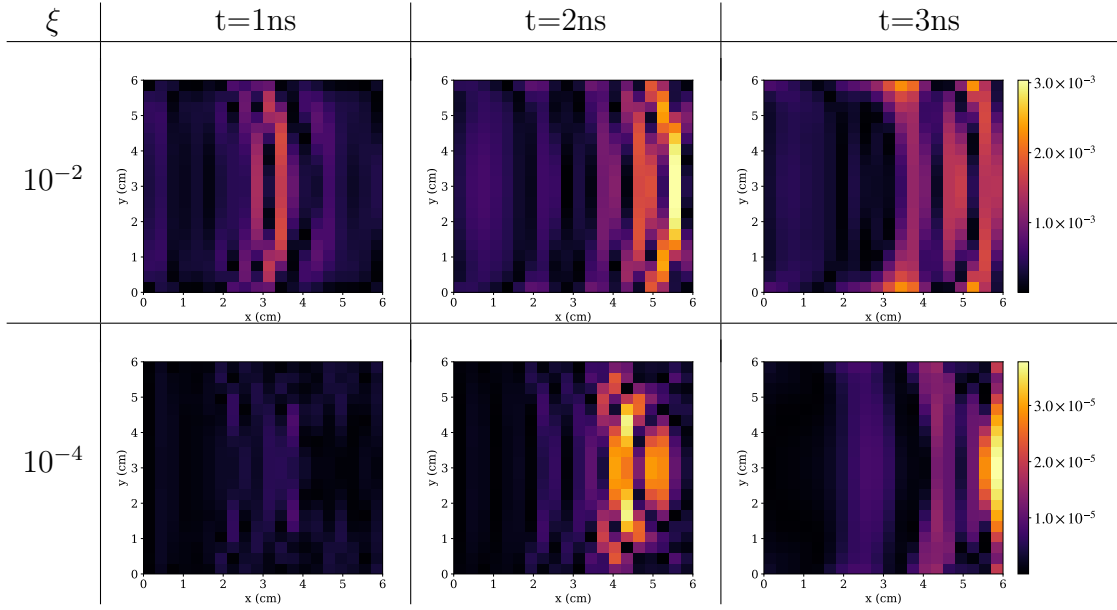
(a) Material Temperature



(b) Radiation Energy Density

Figure 14: Cell-wise relative error in material temperature ($T$) and total radiation energy density ($E$) over the spatial domain at times t=1, 2, 3 ns for the DET ROM equipped with the DMD for $\xi = 10^{-2}, 10^{-4}$.

(a) Material Temperature



(b) Radiation Energy Density

Figure 15: Cell-wise relative error in material temperature ($T$) and total radiation energy density ($E$) over the spatial domain at times t=1, 2, 3 ns for the DET ROM equipped with the DMD-E for $\xi = 10^{-2}, 10^{-4}$.
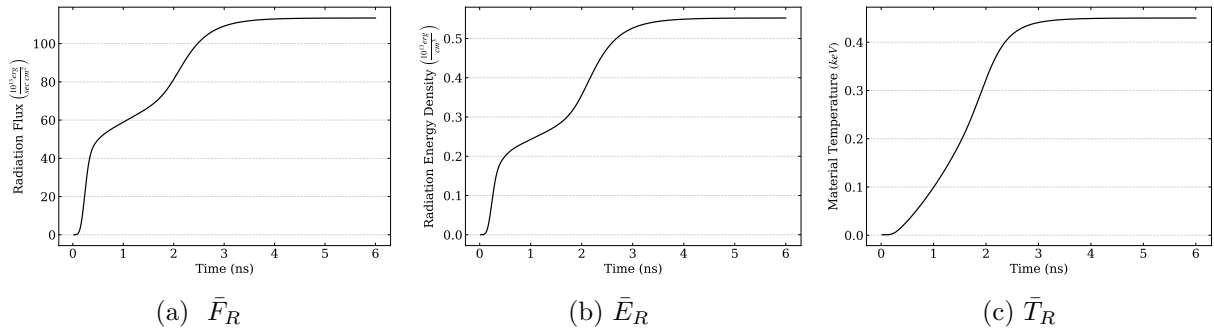
Figure 16: Total radiation flux ($\bar{F}_R$), total radiation energy density ($\bar{E}_R$) and material temperature ($\bar{T}_R$) averaged over the right boundary of the spatial domain plotted vs time. Shown solutions are generated by the FOM.

Figures 17 and 18 plot the relative error in each of these quantities produced by the DET ROMs using the POD, DMD and DMD-E with a very low rank corresponding to $\xi = 10^{-2}, 10^{-4}$, respectively. In a similar manner to the results shown above, the DET ROM with the DMD is observed to reproduce the FOM with the lowest accuracy and the ROMs with the POD and DMD-E achieve similar levels of error to one another. High accuracy is achieved for all considered ROMs with the highest errors on the order of $10^{-2}$. When using the POD or DMD-E even with $\xi = 10^{-2}$, the relative error is about $10^{-3}$.

These results show that the low-rank DET ROMs generate predictions of the temperature and radiation wave propagations with accuracy sufficient for practical simulations. In the vast majority of cases each of these ROMs yielded the same time step as the FOM for when either $\bar{F}_R$, $\bar{E}_R$, and $\bar{T}_R$ reached a certain arbitrary value.
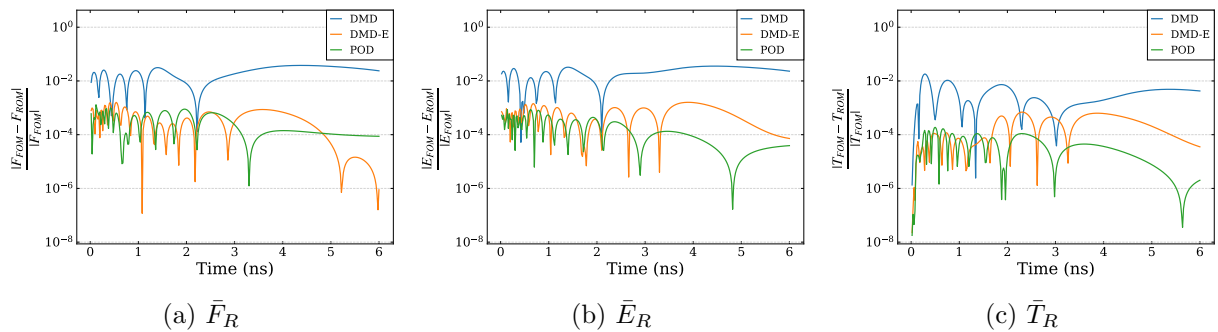


Figure 17: Relative error for the DET ROMs with $\xi = 10^{-2}$ for data located at and integrated over the right boundary of the domain.
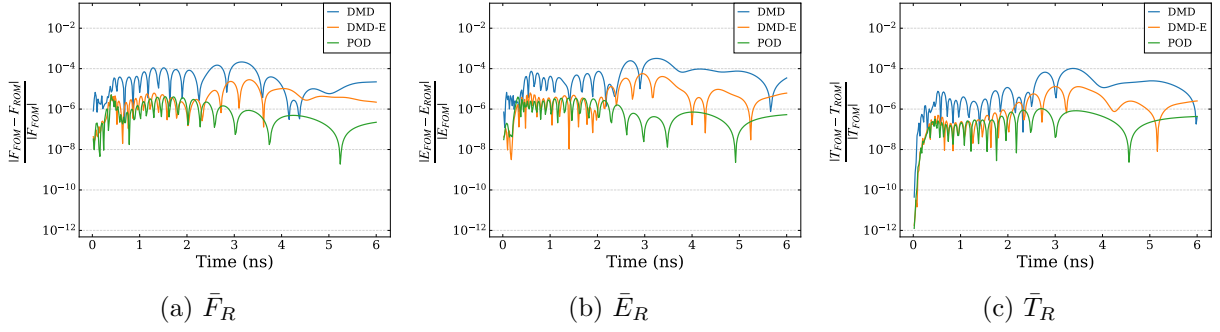
Figure 18: Relative error for the DET ROMs with $\xi = 10^{-4}$ for data located at and integrated over the right boundary of the domain.

## 7. A Parameterization of the DET ROMs

### 7.1. Dimensionless Equations for Grey TRT Problems

In order to identify an appropriate parameterization of the DET ROMs for the target class of TRT problems, we nondimensionalize the following grey TRT problem to analyze its dependencies on parameters of interest:

$$\frac{1}{c}\frac{\partial \tilde{I}}{\partial t} + \mathbf{\Omega} \cdot \mathbf{\nabla}\tilde{I} + \tilde{\varkappa}(T)\tilde{I} = \tilde{\varkappa}(T)B(T), \tag{48}$$

$$\mathbf{r} \in \Gamma, \quad \mathbf{\Omega} \in \mathcal{S}, \quad t \in [0, t_{end}],$$

$$\tilde{I}\big|_{\mathbf{r} \in \partial\Gamma} = \frac{1}{4\pi}B(T^{in}) \text{ for } \mathbf{\Omega} \cdot \mathbf{e}_n < 0, \quad \tilde{I}\big|_{t=0} = \frac{1}{4\pi}B(T^0), \tag{49}$$

$$\frac{\partial \varepsilon(T)}{\partial t} = \tilde{\varkappa}(T)\left(\int_{4\pi} \tilde{I}d\Omega - 4\pi B(T)\right), \tag{50}$$

$$T\big|_{t=0} = T^0. \tag{51}$$

Here $\tilde{I} = \tilde{I}(\mathbf{r}, \mathbf{\Omega}, t)$ is the grey intensity, $\tilde{\varkappa}$ is the grey opacity, and

$$B(T) = \int_0^\infty B(\nu, T) \, d\nu = \frac{ca_R}{4\pi}T^4 \tag{52}$$

is the Planckian function, where $B(\nu, T)$ is defined in Eq. (7). The LOQD equations for $\tilde{E} = \frac{1}{c}\int_{4\pi}\tilde{I}d\Omega$ and $\tilde{\mathbf{F}} = \int_{4\pi}\mathbf{\Omega}\tilde{I}d\Omega$ are given by

$$\frac{\partial \tilde{E}}{\partial t} + \mathbf{\nabla} \cdot \tilde{\mathbf{F}} + c\tilde{\varkappa}(T)\tilde{E} = 4\pi\tilde{\varkappa}(T)B(T), \tag{53a}$$

$$\frac{1}{c}\frac{\partial \tilde{\mathbf{F}}}{\partial t} + c\mathbf{\nabla} \cdot (\tilde{\mathfrak{f}}\tilde{E}) + \tilde{\varkappa}(T)\tilde{\mathbf{F}} = 0, \tag{53b}$$

$$\mathbf{e}_n \cdot \tilde{\mathbf{F}}\big|_{\mathbf{r} \in \partial\Gamma} = c\tilde{C}\left(\tilde{E}\big|_{\mathbf{r} \in \partial\Gamma} - \frac{\alpha_0}{c}B(T^{in})\right) + \alpha_1 B(T^{in}), \tag{53c}$$

$$\tilde{E}\big|_{t=0} = \frac{1}{c}B(T^0), \quad \tilde{\mathbf{F}}\big|_{t=0} = 0, \tag{53d}$$

28

where

$$\tilde{\mathfrak{f}}[\tilde{I}] = \frac{\int_{4\pi} \boldsymbol{\Omega} \otimes \boldsymbol{\Omega} \tilde{I} \ d\Omega}{\int_{4\pi} \tilde{I} d\Omega}, \qquad (54)$$

$$\tilde{C}[\tilde{I}] = \frac{\int_{\boldsymbol{\Omega}\cdot\boldsymbol{e}_n>0} \boldsymbol{e}_n \cdot \boldsymbol{\Omega} \tilde{I} \ d\Omega}{\int_{\boldsymbol{\Omega}\cdot\boldsymbol{e}_n>0} \tilde{I} \ d\Omega}\Bigg|_{\boldsymbol{r}\in\partial\Gamma}, \qquad (55)$$

$$\alpha_k = \int_{\boldsymbol{\Omega}\cdot\boldsymbol{e}_n<0} (\boldsymbol{e}_n \cdot \boldsymbol{\Omega})^k d\Omega\big|_{\boldsymbol{r}\in\partial\Gamma}, \quad k = 0, 1\,. \qquad (56)$$

These equations are coupled with the MEB equation defined by

$$\frac{\partial \varepsilon(T)}{\partial t} = \tilde{\varkappa}(T)\big(c\tilde{E} - 4\pi B(T)\big). \qquad (57)$$

To derive a dimensionless system of equations from Eqs. (48), (53) and (57) we change variables using the characteristic length scale $\mathfrak{L}$ of the spatial domain and temperature scale $\hat{T}$. We consider the case with a linear material energy density

$$\varepsilon(T) = c_v T, \qquad (58)$$

and an opacity function of the following form:

$$\varkappa(T) = \frac{\varkappa_0}{T^p}, \quad p \geq 0, \qquad (59)$$

where $\varkappa_0$ is some constant. Dimensionless spatial and temporal variables are defined as

$$\boldsymbol{\rho} = \frac{\boldsymbol{r}}{\mathfrak{L}}, \quad \tau = \frac{c}{\mathfrak{L}}t. \qquad (60)$$

Dimensionless dependent variables are given by

$$\mathfrak{I}(\boldsymbol{\rho}, \boldsymbol{\Omega}, \tau) = \frac{\tilde{I}(\boldsymbol{r}, \boldsymbol{\Omega}, t)}{\hat{B}}, \quad \mathfrak{E}(\boldsymbol{\rho}, \tau) = c\frac{\tilde{E}(\boldsymbol{r}, t)}{4\pi\hat{B}}, \quad \mathfrak{F}(\boldsymbol{\rho}, \tau) = \frac{\tilde{\boldsymbol{F}}(\boldsymbol{r}, t)}{4\pi\hat{B}}, \quad \theta(\boldsymbol{\rho}, \tau) = \frac{T(\boldsymbol{r}, t)}{\hat{T}}, \quad (61)$$

where

$$\hat{B} = B(\hat{T}). \qquad (62)$$

Lastly we introduce the following dimensionless coefficients:

$$\sigma = \frac{\mathfrak{L}\varkappa_0}{\hat{T}^p}, \quad \eta = \frac{c_v}{a_R\hat{T}^3}\,. \qquad (63)$$

We apply change of variables defined by Eq. (61) in the grey BTE (Eq. (48)) to obtain

$$\frac{\hat{B}}{\mathfrak{L}}\left(\frac{\partial \mathfrak{I}}{\partial \tau} + \boldsymbol{\Omega} \cdot \boldsymbol{\nabla}_\rho \mathfrak{I}\right) + \frac{\varkappa_0}{\hat{T}^p\theta^p}\hat{B}\mathfrak{I} = \frac{\varkappa_0}{\hat{T}^p\theta^p}B(T)\,. \qquad (64)$$

29

As a result, the dimensionless BTE has the following form:

$$\frac{\partial \mathfrak{I}}{\partial \tau} + \boldsymbol{\Omega} \cdot \boldsymbol{\nabla}_\rho \mathfrak{I} + \frac{\sigma}{\theta^p} \mathfrak{I} = \frac{\sigma}{\theta^p} \beta(\theta), \quad \boldsymbol{\rho} \in \Lambda, \quad \boldsymbol{\Omega} \in \mathcal{S}, \quad \tau \geq 0 \tag{65}$$

with the BC and IC given by

$$\mathfrak{I}\big|_{\boldsymbol{\rho} \in \partial \Lambda} = \frac{1}{4\pi} \beta(\theta^{in}) \text{ for } \boldsymbol{\Omega} \cdot \boldsymbol{e}_n < 0, \quad \mathfrak{I}\big|_{\tau=0} = \frac{1}{4\pi} \beta(\theta^0), \tag{66}$$

where $\Lambda$ is the scaled spatial domain,

$$\beta(\theta) = \frac{B}{\hat{B}} = \theta^4, \quad \theta^{in} = \frac{T^{in}}{\hat{T}}, \quad \theta^0 = \frac{T^0}{\hat{T}}. \tag{67}$$

A change of variables is performed on the radiation energy balance equation (Eq. (53a)) to get

$$\frac{\hat{B}}{\mathfrak{L}} \left( \frac{\partial \mathfrak{E}}{\partial \tau} + \boldsymbol{\nabla}_\rho \cdot \mathfrak{F} \right) + \frac{\varkappa_0}{\hat{T}^p \theta^p} \hat{B} \mathfrak{E} = \frac{\varkappa_0}{\hat{T}^p \theta^p} B, \tag{68}$$

which when recombined becomes the dimensionless radiation energy balance equation

$$\frac{\partial \mathfrak{E}}{\partial \tau} + \boldsymbol{\nabla}_\rho \cdot \mathfrak{F} + \frac{\sigma}{\theta^p} \mathfrak{E} = \frac{\sigma}{\theta^p} \beta(\theta). \tag{69}$$

The variables in Eq. (61) are similarly substituted into the radiation momentum balance equation (Eq. (53b)) to find

$$\frac{\hat{B}}{\mathfrak{L}} \left( \frac{\partial \mathfrak{F}}{\partial \tau} + \boldsymbol{\nabla}_\rho \cdot (\tilde{\mathfrak{f}} \mathfrak{E}) \right) + \frac{\varkappa_0 \hat{B}}{\hat{T}^p \theta^p} \mathfrak{F} = 0, \tag{70}$$

which gives rise to the dimensionless radiation momentum balance equation

$$\frac{\partial \mathfrak{F}}{\partial \tau} + \boldsymbol{\nabla}_\rho \cdot (\tilde{\mathfrak{f}} \mathfrak{E}) + \frac{\sigma}{\theta^p} \mathfrak{F} = 0. \tag{71}$$

The BC and IC are defined by

$$\boldsymbol{e}_n \cdot \mathfrak{F}\big|_{\boldsymbol{\rho} \in \partial \Lambda} = c\tilde{C} \left( \mathfrak{E}\big|_{\boldsymbol{\rho} \in \partial \Lambda} - \frac{\alpha_0}{4\pi c} \beta(\theta^{in}) \right) + \frac{\alpha_1}{4\pi} \beta(\theta^{in}), \tag{72}$$

$$\mathfrak{E}\big|_{\tau=0} = \frac{1}{4\pi c} \beta(\theta^0), \quad \mathfrak{F}\big|_{\tau=0} = 0. \tag{73}$$

The Eddington tensor $\tilde{\mathfrak{f}}$ and boundary factor $\tilde{C}$ are dimensionless quantities by definition (Eqs. (54) and (55)) and

$$\tilde{\mathfrak{f}}[\tilde{I}] = \tilde{\mathfrak{f}}[\mathfrak{I}], \quad \tilde{C}[\tilde{I}] = \tilde{C}[\mathfrak{I}]. \tag{74}$$

The change of variables applied to the MEB equation (Eq. (57)) with a material energy density of the form in Eq. (58) yields

$$\frac{c_v c \hat{T}}{\mathfrak{L}} \frac{\partial \theta}{\partial \tau} = \frac{4\pi \varkappa_0}{\hat{T}^p \theta^p} (\hat{B} \mathfrak{E} - B). \tag{75}$$

30

which leads to the dimensionless MEB equation given by

$$\eta \frac{\partial \theta}{\partial \tau} = \frac{\sigma}{\theta^p}(\mathfrak{E} - \beta(\theta)), \quad \theta\big|_{\tau=0} = \theta^0. \tag{76}$$

Equations (65), (69), (71), and (76) with corresponding BCs and ICs comprise a dimensionless description of the grey TRT problem. We notice that these equations depend on parameter $\sigma$ defined in Eq. (63).

We now consider the F-C test defined in Section 6.2. The spectral opacity $\varkappa(\nu, T)$ in this test is given by Eq. (45). The characteristic grey opacity can be evaluated as

$$\varkappa(T) = \frac{\int_0^\infty \varkappa(\nu, T) B(\nu, T) \, d\nu}{\int_0^\infty B(\nu, T) \, d\nu}, \tag{77}$$

which results in

$$\varkappa(T) = \frac{\tilde{\varkappa}_0}{T^3}, \tag{78}$$

where

$$\tilde{\varkappa}_0 = \frac{15\varkappa^*}{\pi^4} \left[\frac{\text{KeV}^3}{\text{cm}}\right], \tag{79}$$

and $\varkappa^* = 27$ is a parameter of the F-C test. Thus, in the F-C test $p = 3$.

In the next section, we perform parametrization of the DET ROM for the F-C problem with respect to the temperature of incoming radiation $T^{\text{in}}$. We choose the characteristic temperature $\hat{T} = T^{\text{in}}$. As a result, the parameter $\sigma$ of the dimensionless grey TRT problem varies versus characteristic temperature of the problem as $(T^{\text{in}})^{-3}$. Note that BCs (66) and (72) are independent of the temperature of incoming radiation due to $\beta(T^{\text{in}}) = 1$.

### 7.2. Numerical Results

The F-C test (see Section 6.2) mimics the class of supersonic radiation shock problems and experiments [81, 82, 83, 84], with radiation flowing from the high-temperature 'drive' at the left boundary to the cold right boundary. It is therefore natural to define the characteristic temperature $\hat{T}$ as the temperature of incoming radiation (radiation drive temperature) $T^{\text{in}}$. In this section a parameterization of the DET ROMs is analyzed using the single parameter $\vartheta = T^{\text{in}}$. We develop interpolation-based ROM defined for the time interval with $t_{end} = 6$ ns. The space of considered parameter values is set to the interval $\Theta \equiv [0.5, 1.5\text{KeV}]$. The interpolation function $\mathcal{I}(\vartheta)$ (see Eq. (44)) is set to a natural cubic spline.

The interval of $T^{\text{in}} \in [0.5, 1.5\text{KeV}]$ is chosen to test the parametrized DET ROMs. This interval is a large one, covering 1 KeV of change between the possible values of the boundary temperature (or radiation drive). The F-C test's physics change over this range. The spectrum of radiation formed by the left-boundary condition has its peak at $\nu = 2.82T^{\text{in}}$. Therefore the bulk of radiation that forms the wavefront propagating through the test domain varies over a 1 KeV range as well. Evaluating the characteristic grey opacity (Eq. (78)) over the interval of considered drive temperatures gives that $\varkappa|_{T=0.5} = 27\varkappa|_{T=1.5}$. As such

different portions of this drive temperature range will result in distinct, separate physical characterizations of the F-C test in space-time.

It is worth noting that in the parameterized case, the only additional source of error to the DET ROM solution compared to the non-parameterized case comes from $\mathcal{I}(\vartheta)$. As such for any well-chosen interpolation function and a fine enough grid in $\vartheta$, the parameterized DET ROM's behavior will be the same as shown in Section 6. In practice coarse parameter grids are desirable, and it is most important to identify $\mathcal{I}(\vartheta)$ that can introduce errors on the level less than observed for the non-parameterized DET ROMs with low rank ($\xi = 10^{-2}, 10^{-4}$). In this way the parameterized DET ROM can produce solutions for unsampled parameter values with similar levels of error as for the non-parameterized case with low rank.

The dimensionless analysis from Section 7.1 suggests a parameterization over $\tilde{\vartheta}^{in} = 1/(T^{in})^3$. Therefore we apply a natural cubic spline interpolant of $\tilde{\vartheta}^{in}$ (i.e. $\mathcal{I}((T^{in})^{-3})$) when interpolating between FOM solutions in our database. A sampling scheme must also be identified to select the FOM parameter values $\{\tilde{\vartheta}^{in}_\ell\}_{\ell=1}^L \subset \boldsymbol{\Theta}$ which are used to form the database of solutions. Analysis showed that a sampling scheme that can provide accuracy close in its order of magnitude for the parameterized DET ROMs across the whole interval $\tilde{\vartheta}^{in} \in [1.5^{-3}, 8]$ should handle intervals $\tilde{\vartheta}^{in} \in [1.5^{-3}, 1]$ and $\tilde{\vartheta}^{in} \in [1, 8]$ differently. We select the points uniformly distributed over $\tilde{\vartheta} \in [1, 8]$. The high-energy subinterval $\tilde{\vartheta}^{in} \in [1.5^{-3}, 1]$ can have a coarser sampled grid. Analysis of various variants of sampling for the high-energy portion of the interval showed also that for the interval $\tilde{\vartheta}^{in} \in [1.5^{-3}, 1]$ uniform sampling with respect to $(\tilde{\vartheta}^{in})^{-3}$ gives better results.

| $\ell$ | $\tilde{\vartheta}^{in}_\ell$ | $T^{in}_\ell$ [KeV] |
|---|---|---|
| 1 | 0.296 | 1.5 |
| 2 | 0.512 | 1.25 |
| 3 | 1.0 | 1.0 |
| 4 | 2.75 | 0.714 |
| 5 | 4.49 | 0.606 |
| 6 | 6.25 | 0.543 |
| 7 | 8.0 | 0.5 |

(a) $L = 7$

| $\ell$ | $\tilde{\vartheta}^{in}_\ell$ | $T^{in}_\ell$ [KeV] | $\ell$ | $\tilde{\vartheta}^{in}_\ell$ | $T^{in}_\ell$ [KeV] |
|---|---|---|---|---|---|
| 1 | 0.296 | 1.5 | 8 | 3.62 | 0.651 |
| 2 | 0.385 | 1.375 | 9 | 4.49 | 0.606 |
| 3 | 0.512 | 1.25 | 10 | 5.37 | 0.571 |
| 4 | 0.702 | 1.125 | 11 | 6.25 | 0.543 |
| 5 | 1.0 | 1.0 | 12 | 7.11 | 0.520 |
| 6 | 1.87 | 0.811 | 13 | 8.0 | 0.5 |
| 7 | 2.75 | 0.714 | | | |

(b) $L = 13$

Table 5: Grids in $\tilde{\vartheta}^{in} = (T^{in})^{-3}$ for parameterized DET ROMs with 7 and 13 points

Table 5 presents the sampled points in $T^{in}$ for this scheme with 2 levels of refinement. A grid with $L = 7$ is presented, where 3 points are used to sample the high-energy subinterval and 5 points are used in the low-energy subinterval. The second grid with $L = 13$ uses 5 and 9 points in the high and low energy subintervals, respectively. The test points where the parameterized DET ROMs will be evaluated for error analysis are shown in Table 6. These test points are defined to be equidistant between each adjacent sampling point in the inverse cubic and linear senses for the low and high energy subintervals, respectively.

Figures 19 and 20 plot the relative errors in the material temperature and total radiation

| $\ell$ | $\tilde{\vartheta}_\ell^{\text{in}}$ | $T_\ell^{\text{in}}$ [KeV] |
|---|---|---|
| 1 | 0.385 | 1.375 |
| 2 | 0.702 | 1.125 |
| 3 | 1.87 | 0.811 |
| 4 | 3.62 | 0.651 |
| 5 | 5.37 | 0.571 |
| 6 | 7.11 | 0.520 |

(a) $L = 7$

| $\ell$ | $\tilde{\vartheta}_\ell^{\text{in}}$ | $T_\ell^{\text{in}}$ [KeV] | $\ell$ | $\tilde{\vartheta}_\ell^{\text{in}}$ | $T_\ell^{\text{in}}$ [KeV] |
|---|---|---|---|---|---|
| 1 | 0.366 | 1.438 | 7 | 3.19 | 0.679 |
| 2 | 0.442 | 1.313 | 8 | 4.06 | 0.627 |
| 3 | 0.596 | 1.188 | 9 | 4.94 | 0.587 |
| 4 | 0.833 | 1.063 | 10 | 5.82 | 0.556 |
| 5 | 1.44 | 0.886 | 11 | 6.68 | 0.531 |
| 6 | 2.31 | 0.756 | 12 | 7.58 | 0.509 |

(b) $L = 13$

Table 6: Test points for $\tilde{\vartheta}^{\text{in}}$ to evaluate the parameterized DET ROMs with 7 and 13 points.

energy density in the 2-norm over space produced by the parameterized DET ROM using $\xi = 10^{-2}$ and $\xi = 10^{-4}$ respectively at the 7-point grid test points shown in Table 6. Errors are calculated relative to the FOM solution for the same value of $T^{\text{in}}$. In both cases the interpolation function $\mathcal{I}(\tilde{\vartheta})$ is used, defined for the sampled points in the 7-point grid shown in Table 5. The error levels for both $T$ and $E$ at every tested value for $T^{\text{in}}$ are bounded by roughly $2 \times 10^{-3}$ and reside in a close interval to one another at each instant of time. The tested values for $T^{\text{in}} > 1$ KeV have greater accuracy than those values for $T^{\text{in}} < 1$ KeV in general during the interval $t \geq 1$ ns with the exception of $T^{\text{in}} = 0.811$ KeV. For $\xi = 10^{-2}$ the errors vs. time are close to those seen for the non-parameterized case (see Figure 7), and when $\xi = 10^{-4}$ these error values decrease in the range $t \leq 2$ ns.

Figures 21 and 22 plot the relative errors in the material temperature and total radiation energy density in the 2-norm over space produced by the parameterized DET ROM using $\xi = 10^{-2}$ and $\xi = 10^{-4}$ respectively at the 13-point grid test points shown in Table 6. In both cases the interpolation function $\mathcal{I}(\tilde{\vartheta})$ is used, defined for the sampled points in the 13-point grid shown in Table 5. Here the error levels across time are the same as seen for the non-parameterized case for all tested $T^{\text{in}}$ when $\xi = 10^{-2}$. All error levels decrease when $\xi = 10^{-4}$. The points when $T^{\text{in}} > 1$ KeV are observed to decrease somewhat uniformly in time with $\xi$, and the points for $T^{\text{in}} < 1$ KeV decrease more significantly at early times, increasing with time until roughly $t = 3$ ns where a plateau around $10^{-4}$ is reached.
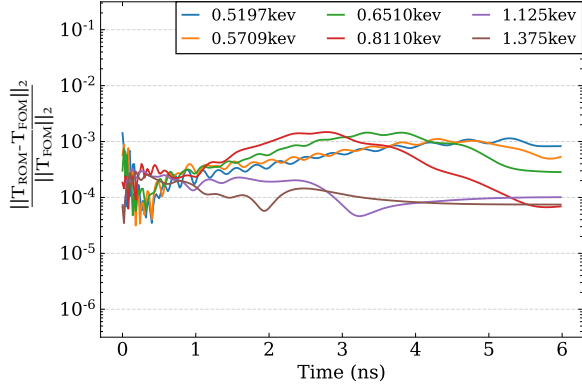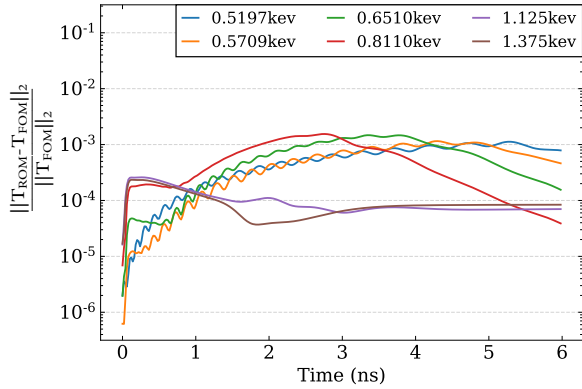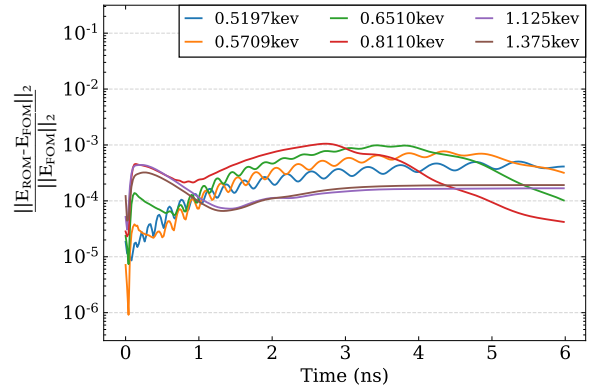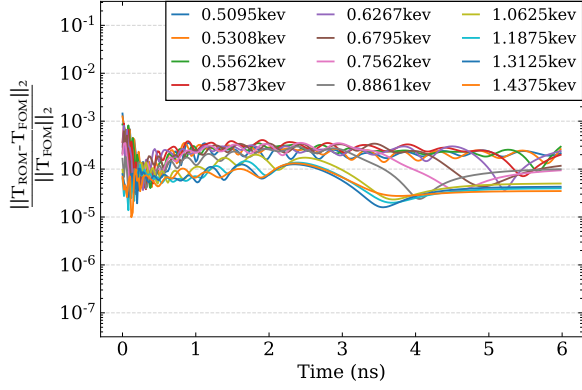
(a) Material Temperature
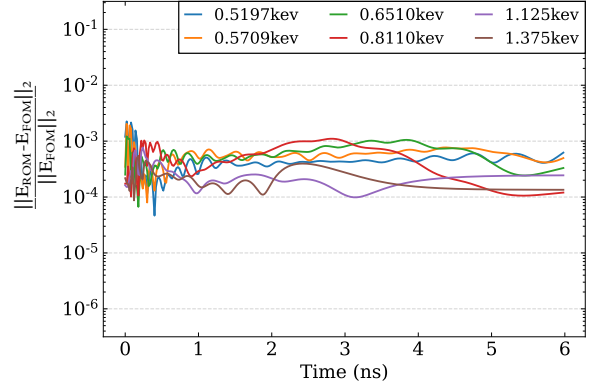
(b) Radiation Energy Density

Figure 19: Relative errors in the 2-norm of the DET ROM with the POD and $\xi = 10^{-2}$, evaluated at the $T^{\mathrm{in}}$ values in Table 6 with the interpolation function over $\tilde{\vartheta}^{\mathrm{in}} = (T^{\mathrm{in}})^{-3}$ defined for the values shown in Table 5 for $L = 7$. Errors are plotted vs. time
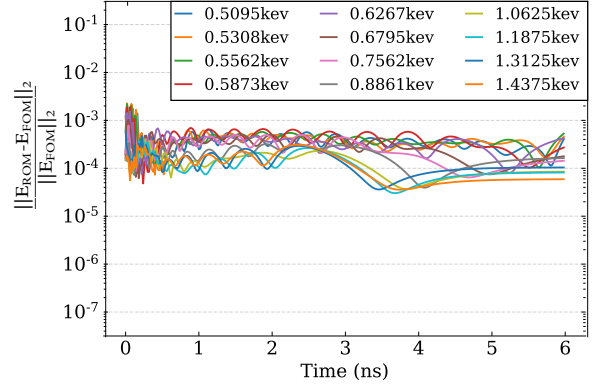


(a) Material Temperature

(b) Radiation Energy Density

Figure 20: Relative errors in the 2-norm of the DET ROM with the POD and $\xi = 10^{-4}$, evaluated at the $T^{\mathrm{in}}$ values in Table 6 with the interpolation function over $\tilde{\vartheta}^{\mathrm{in}} = (T^{\mathrm{in}})^{-3}$ defined for the values shown in Table 5 for $L = 7$. Errors are plotted vs. time
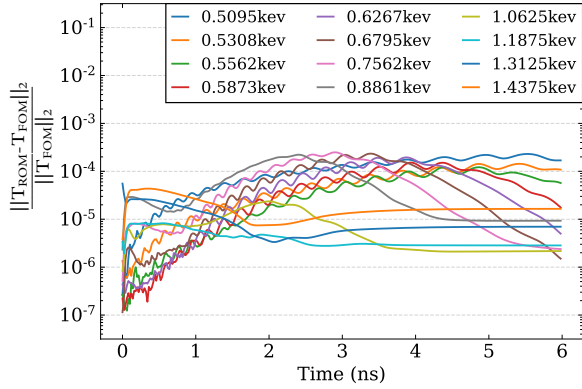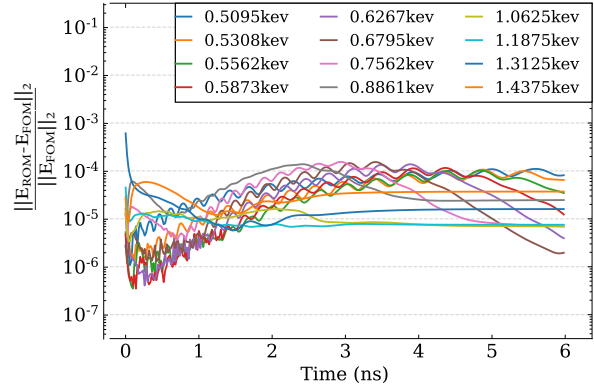
34

(a) Material Temperature

(b) Radiation Energy Density

Figure 21: Relative errors in the 2-norm of the DET ROM with the POD and $\xi = 10^{-2}$, evaluated at the $T^{\text{in}}$ values in Table 6 with the interpolation function over $\tilde{\vartheta}^{\text{in}} = (T^{\text{in}})^{-3}$ defined for the values shown in Table 5 for $L = 13$. Errors are plotted vs. time



(a) Material Temperature

(b) Radiation Energy Density

Figure 22: Relative errors in the 2-norm of the DET ROM with the POD and $\xi = 10^{-4}$, evaluated at the $T^{\text{in}}$ values in Table 6 with the interpolation function over $\tilde{\vartheta}^{\text{in}} = (T^{\text{in}})^{-3}$ defined for the values shown in Table 5 for $L = 13$. Errors are plotted vs. time

## 8. Conclusion

In this paper, new structure and asymptotic preserving ROMs for TRT problems are presented. The DET ROMs are formulated by a multilevel system of moment equations derived by means of the nonlinear-projective approach. The exact closures of the radiation pressure tensor in the moment equations are formulated by the group Eddington (QD) tensor defined by the specific intensity. The proposed ROMs employ data-driven approximations for the group Eddington tensor based on available data to formulate approximate closures. Three data compression techniques are applied, namely, POD, DMD and DMD-E. The low-rank approximation of the group Eddington tensor is performed over the whole phase space and time interval. The hierarchy of moment equations include radiation energy and momentum balance equations. These equations are discretized by conservative discretization schemes. The solution of the discretized moment equations satisfies the corresponding conservation laws.

Analysis of the DET ROMs has been performed on the classical Fleck-Cummings TRT multigroup test problem with a radiation-driven Marshak wave. The ROMs were proven effective in reducing dimensionality of TRT problems and shown capable of producing solutions with a spectrum of accuracy depending on the used rank of approximation. A linear relationship was observed between the ROM solution accuracy and the rank of approximation while using the POD and DMD, allowing for a-priori predictions of the ROM solution error levels based on the rank parameter $\xi$. The DET ROMs have been applied to develop a parameterized ROM for a class of TRT problems. Parameterization was investigated for temperature of incoming radiation at the boundary that drives the Marshak wave. Analysis of a dimensionless grey TRT problem has been used to identify elements of database representation. An inverse cubic parameterization in the incoming radiation temperature was shown to produce solutions with relatively uniform accuracy across the entire considered interval of temperatures.

The POD ROM closely matches the DMD-E ROM for low-rank approximations, and is more accurate than either DMD ROM for high-rank approximations, although the DMD ROMs have the strength of being continuous in time. If the POD ROM is to be applied to a different set of time steps than those used to generate the training data, an interpolation scheme must be defined on the training grid of time instances and used to generate new data for the new values of time steps $\Delta t$ [108]. A possible technique to overcome the shortcomings of both DMD ROMs would be to combine them such that the DMD-E ROM is used for low-rank approximations and the DMD is used instead for high-rank approximations. This would produce a DMD-based DET ROM with accuracy similar to the POD ROM while using low-rank that is able to converge as the rank is increased.

The results and analysis of the DET ROMs encourage continued development, and several pathways for future research can be identified. The ROM parameterization can be extended to the multivariate case applying advanced data sampling techniques [109, 110]. Methods of symmetry reduction [111, 112] can also be applied to improve efficiency of the Eddington tensor approximation The proposed approach for development of ROMs has a potential for application to different multiphysical high-energy density problems.

## 9. Acknowledgements

## References

[1] F. H. Shu, The physics of astrophysics, University Science Books, 1991.

[2] G. E. Thomas, K. Stamnes, Radiative Transfer in the Atmosphere and Ocean, Cambridge, 1999.

[3] M. Faghri, B. Sundén, Transport Phenomena in Fires, volume 20 of *Developments in Heat Transfer*, WIT, 2008.

[4] R. P. Drake, High-Energy-Density-Physics: Foundation of Interial Fusion and Experimental Astrophysics, Springer, 2018.

[5] G. L. Olson, L. H. Auer and M. L. Hall, Diffusion, $P_1$, and other approximate forms of radiation transport, Journal of Quantitative Spectroscopy & Radiative Transfer 64 (2000) 619–634.

[6] J. E. Morel, Diffusion-limit asymptotics of the transport equation, the $P_{1/3}$ equations, and two flux-limited diffusion theories, Journal of Quantitative Spectroscopy & Radiative Transfer 65 (2000) 769–778.

[7] K. H. Simmons, D. Mihalas, A linearized analysis of the modified $P_1$ equations, Journal of Quantitative Spectroscopy & Radiative Transfer 66 (2000) 263–269.

[8] C. D. Levermore, Moment closure hierarchies for kinetic theories, Journal of Statistical Physics 83 (1996) 1021–1065.

[9] C. D. Hauck, High-order entropy-based closures for linear transport in slab geometry, Communications in Mathematical Sciences 9 (2011) 187–205.

[10] G. W. Alldredge, C. D. Hauck, A. L. Tits, High-order entropy-based closures for linear transport in slab geometry II: A computational study of the optimization problem, SIAM Journal on Scientific Computing 34 (2012) B361–B391.

[11] D. S. Kershaw, Flux limiting nature's own way – A new method for numerical solution of the transport equation, Technical Report, Lawrence Livermore National Laboratory, Livermore, CA, 1976.

[12] J. M. LeBlanc, J. R. Wilson, Analytic closures for m1 neutrino transport, The Astrophysical Journal 161 (1970) 541–551.

[13] C. D. Levermore, Relating Eddington factors to flux limiters, Journal of Quantitative Spectroscopy & Radiative Transfer 31 (1984) 149–160.

[14] E. M. Murchikova, E. Abdikamalov, T. Urbatsch, Analytic closures for M1 neutrino transport, Monthly Notices of the Royal Astronomical Society 469 (2017) 1725–1737.

[15] D. J. Lucia, P. S. Beran and W. A. Silva, Reduced-order modeling: New approaches for computational physics, Progress in Aerospace Sciences 40 (2004) 51–117.

[16] T. Hastie, R. Tibshirani and J. Friedman, The elements of statistical learning, Springer, 2009.

[17] P. Benner, S. Gugercin and K. Willcox, A survey of projection-based model reduction methods for parametric dynamical systems, SIAM Review 57 (2015) 483–531.

[18] S. L. Brunton, J. N. Kutz, Data-Driven Science and Engineering, Cambridge, 2019.

[19] P. Benner, S. Givet-Talocia, A. Quarteroni, G. Rozza, W. Schilders, L. M. Silveria, Model Order Reduction: Volume 2: Snapshot-Based Methods and Algorithms, De Gruyter, 2020.

[20] J. L. Lumley, The structure of inhomogeneous turbulent flows, in: A. M. Yaglmo, V. I. Takarski (Eds.), Atmospheric Turbulence and Radio Wave Propagation, 1967, pp. 166–178.

[21] L. Sirovich, Turbulence and the dynamics of coherent structures, parts i-iii, Quarterly of Applied Mathematics XLV (1987) 561–590.

[22] L. Sirovich, Chaotic dynamics of coherent structures, Physica D 37 (1989) 126–145.

[23] N. Aubry, The hidden beauty of the proper orthogonal decomposition, Theoretical and Computational Fluid Dynamics 2 (1991) 339–352.

[24] G. Berkooz, P. Holmes and J. L. Lumley, The proper orthogonal decomposition in the analysis of turbulent flows, Annual Review of Fluid Mechanics 25 (1993) 539–575.

[25] P. Holmes, J. L. Lumley, G. Berkooz, Coherent Structures, Dynamical Systems and Symmetry, Cambridge University Press,, Cambridge, 1996.

[26] C. W. Rowley, I. Mezić, S. Bagheri, P. Schlatter, D. S. Henningson, Spectral analysis of nonlinear flows, J. Fluid Mech 641 (2009) 115–127.

[27] P. J. Schmid, Dynamic mode decomposition of numerical and experimental data, Journal of Fluid Mechanics 656 (2010) 5–28.

[28] J. H. Tu, C. W. Rowley, D. M. Luchtenburg, S. L. Brunton and J. N. Kutz, On dynamic mode decomposition: Theory and applications, Journal of Computational Dynamics 1 (2014) 391–421.

[29] M. O. Williams, I. G. Kevrekidis and C. W. Rowley, A data-driven approximation of the Koopman operator: Extending dynamic mode decomposition, Journal of Nonlinear Science 25 (2015) 1307–1346.

[30] I. Goodfellow, Y. Bengio and A. Courville, Deep Learning, MIT Press, 2016.

[31] F. Chinesta, A. Ammar, A. Laygue and R. Keunings, An overview of the proper generalized decomposition with applications in computational rheology, Journal of Non-Newtonian Fluid Mechanics 166 (2011) 578–592.

[32] B. C. Moore, Principal component analysis in linear systems: controllability, observability, and model reduction, IEEE transactions on automatic control 26 (1981) 17–32.

[33] A. Quarteroni, A. Manzoni and F. Negri, Reduced Basis Methods for Partial Differential Equations: An Introduction, Springer, 2015.

[34] K. Kunisch, S. Volkwein, Galerkin proper orthogonal decomposition methods for a general equation in fluid dynamics, SIAM J. Numer. Anal. 40 (2002) 492–515.

[35] C. W. Rowley, S. T.M. Dawson, Model reduction for flow analysis and control, Annu. Rev. Fluid Mech. 49 (2017) 187–417.

[36] C. W. Rowley, Model reduction for fluids, using balanced proper orthogonal decomposition, International Journal of Bifurcation and Chaos 15 (2004) 997–1013.

[37] C. W. Rowley, T. Colonius and R. M. Murray, Model reduction for compressible flows using POD and Galerkin projection, Physica D 189 (2004) 115–129.

[38] T. R. Smith, J. Moehlis and P. Holmes, Low-dimensional modelling of turbulence using the proper orthogonal decomposition: A tutorial, Nonlinear Dynamics 41 (2005) 275–307.

[39] T. Bui-Thanh, M. Damodaran, K. Willcox, Proper orthogonal decomposition extensions for parametric applications in compressible aerodynamics, in: Proc. of 21st Applied Aerodynamics Conference, 23-28 June 2003, Orlando, FL, 2003, p. 11.

[40] K. Taira, S. L. Brunton, S. T.M. Dawson, C. W. Rowley, T. Colonius, B. J. McKeon, O. T. Schmidt, S. Gordeyev, V. Theofilis and L. S. Ukeiley., Modal analysis of fluid flows: and overview, AIAA Journal 55 (2017) 4013–4041.

[41] A. G. Buchan, A. A. Calloo, M. G. Goffin, S. Dargaville, F. Fang, C. C. Pain, I. M. Navon, A POD reduced order model for resolving angular direction in neutron/photon transport problems, Journal of Computational Physics 296 (2015) 138–157.

[42] J. Tencer, K. Carlberg, M. Larsen, R. Hogan, Accelerated solution of discrete Ordinates approximation to the Boltzmann transport equation for a gray absorbing-emitting medium via model reduction, Journal of Heat Transfer 139 (2017) 122701.

[43] L. Soucasse, A. G. Buchan, S. Dargaville and C. C. Pain, An angular reduced order model for radiative transfer in non grey media, Journal of Quantitative Spectroscopy & Radiative Transfer 229 (2019) 23–32.

[44] Z. Peng, Y. Chen, Y. Cheng, F. Li, A reduced basis method for radiative transfer equation, Journal of Scientific Computing 91 (2022).

[45] A. C. Hughes, A. G. Buchan, An adaptive reduced order model for the angular discretisation of the Boltzmann transport equation using independent basis sets over a partitioning of the space-angle

domain, International Journal for Numerical Methods in Engineering (2022) 1–19.

[46] P. A. Behne, J. C. Ragusa and J. E. Morel, Model order reduction for $S_N$ radiation transport, in: Proc. of Int. Conf. on Mathematics and Computational Methods Applied to Nuclear Science and Engineering (M&C 2019), 2019, p. 10 pp.

[47] P. Behne, J. C. Ragusa, M. Tano, Projection-based parametric model order reduction for transport simulation based on affine decomposition of the operators, in: Proc. of Int. Conf. on Mathematics and Computational Methods Applied to Nuclear Science and Engineering (M&C 2021), 2021, p. 10 pp.

[48] Z. K. Hardy, J. E. Morel and C. Ahrens, Dynamic mode decomposition for subcritical metal systems, in: Proc. of Int. Conf. on Mathematics and Computational Methods Applied to Nuclear Science and Engineering (M&C 2019), 2019, p. 10 pp.

[49] Z. M. Prince and J. C. Ragusa, Proper generalized decomposition of multigroup neutron diffusion with seperated space-energy representation, in: Proc. of Int. Conf. on Mathematics and Computational Methods Applied to Nuclear Science and Engineering (M&C 2019), 2019, p. 10 pp.

[50] K. A. Dominesey, W. Ji, Reduced-order modeling of neutron transport seperated in space and angle via proper generalized decomposition, in: Proc. of Int. Conf. on Mathematics and Computational Methods Applied to Nuclear Science and Engineering (M&C 2019), 2019, p. 10 pp.

[51] Z. M. Prince and J. C. Ragusa, Seperated representation of spatial dimensions in $S_N$ neutron transport using the proper generalized decomposition, in: Proc. of Int. Conf. on Mathematics and Computational Methods Applied to Nuclear Science and Engineering (M&C 2019), 2019, p. 10 pp.

[52] Z. Peng, R. G. McClarren and M. Frank, A low-rank method for time-dependent transport calculations, in: Proc. of Int. Conf. on Mathematics and Computational Methods Applied to Nuclear Science and Engineering (M&C 2019), 2019, p. 10 pp.

[53] Z. Peng, R. McClarren, A high-order / low-order (HOLO) algorithm with low-rank evolution for time-dependent transport calculations, Transactions of the American Nuclear Society 121 (2019) 805–807.

[54] Z. Peng, R. G. McClarren and M. Frank, A low-rank method for two-dimensional time-dependent radiation transport calculations, Journal of Computational Physics 421 (2020) 109735.

[55] Z. Peng and R. G. McClarren, A low-rank method for the discrete ordinate transport equation compatible with transport sweeps, in: Proc. of Int. Conf. on Mathematics and Computational Methods Applied to Nuclear Science and Engineering (M&C 2021), 2021, p. 10 pp.

[56] Y. Choi, P. Brown, W. Arrighi, R. Anderson and K. Huynh, Space-time reduced order model for large-scale linear dynamical systems with application to Boltzmann transport problems, Journal of Computational Physics 424 (2021).

[57] Z. Huang, Y. Chen, A. Christlieb, L. Roberts, Machine learning moment closure models for the radiative transfer equation I: directly learning a gradient based closure, Journal of Computational Physics 453 (2022) 110941.

[58] Z. Huang, Y. Chen, A. Christlieb, L. Roberts, W.-A. Yong, Machine learning moment closure models for the radiative transfer equation II: enforcing global hyperbolicity in gradient based closures, 2021. Preprint on arXiv:2105.14410v1, math.NA.

[59] M. M. Pozulp, 1D transport using neural nets, $S_N$, and MC, in: Proc. of Int. Conf. on Mathematics and Computational Methods Applied to Nuclear Science and Engineering (M&C 2019), 2019, p. 10 pp.

[60] M. M. Pozulp, P. S. Brantley, T. S. Palmer, J. L. Vujic, Heterogeneity, hyperparameters, and GPUs: Towards useful transport calculations using neural networks, in: Proc. of Int. Conf. on Mathematics and Computational Methods Applied to Nuclear Science and Engineering (M&C 2021), 2021, p. 10 pp.

[61] M. H. Elhareef, Z. Wu, Y. Ma, Physics-informed deep learning neural network solution to the neutron diffusion model, in: Proc. of Int. Conf. on Mathematics and Computational Methods Applied to Nuclear Science and Engineering (M&C 2021), 2021, p. 10 pp.

[62] R. Pinnau, A. Schulze, Model reduction techniques for frequency averaging in radiative heat transfer, Journal of Computational Physics 226 (2007) 712–731.

[63] J. Qian, Y. Wang, H. Song, K. Pant, Projection-based reduced-order modeling for spacecraft thermal analysis, Journal of Spacecraft and Rockets 52 (2015) 978–989.

[64] L. Fagiano, R. Gati, On the order reduction of the radiative heat transfer model for the simulation of plasma arcs in switchgear devices, Journal of Quantitative Spectroscopy & Radiative Transfer 169 (2016) 58–78.

[65] A. L. Alberti, T. S. Palmer, Reduced order modeling of non-linear radiation diffusion via proper generalized decomposition, Transactions of the American Nuclear Society 119 (2018) 691–694.

[66] A. L. Alberti, T. S. Palmer, C. J. Palmer, Proper orthogonal decomposition based reduced-order modeling of flux-limited gray thermal radiation, Journal of Quantitative Spectroscopy and Radiative Transfer (2022) 108345. https://doi.org/10.1016/j.jqsrt.2022.108345.

[67] M. Girault, Y. Liu, Y. Billaud, D. Saury, D. Lemonnier, Reduced order models for conduction and radiation inside sem-transparent media via the model identification method, International Journal of Heat and Mass Transfer 168 (2021) 120598.

[68] L. Soucasse, B. Podvin, P. Rivière, A. Soufiani, Reduced-order modelling of radiative transfer effects on Rayleigh-Bénard convection in a cubic cell, J. Fluid Mech. 898 (2020) A2.

[69] L. Soucasse, B. Podvin, P. Rivière, A. Soufiani, Low-order models for predicting radiative transfer effects on Rayleigh-Bénard convection in a cubic cell at different rayleigh numbers, J. Fluid Mech. 917 (2021) A5.

[70] A. Cherezov, R. Sanchez and H. G. Joo, A reduced-basis element method for pin-by-pin reactor core calculations in diffusion and $SP_3$ approximations, Annals of Nuclear Energy 116 (2018) 195–209.

[71] A. L. Alberti and T. S. Palmer, Reduced order modeling of the twigl problem using proper generalized decomposition, in: Proc. of Int. Conf. on Mathematics and Computational Methods Applied to Nuclear Science and Engineering (M&C 2019), 2019, p. 14 pp.

[72] A. L. Alberti and T. S. Palmer, Reduced-order modeling of nuclear reactor kinetics using proper generalized decomposition, Nuclear Science and Engineering 194 (2020) 837–858.

[73] K. A. Dominesey, W. Ji, Reduced-order modeling of neutron transport seperated in energy by proper generalized decomposition with applications to nuclear reactor physics, Journal of Computational Physics 449 (2022) 110744.

[74] P. German, J. C. Ragusa, C. Fiorina, M. T. Retamales, Reduced-order modeling of parameterized multi-physics computations for the molten salt fast reactor, in: Proc. of Int. Conf. on Mathematics and Computational Methods Applied to Nuclear Science and Engineering (M&C 2019), 2019, p. 10 pp.

[75] P. German, J. C. Ragusa, C. Fiorina, Application of multiphysics model order reduction to Doppler/neutronic feedback, Nuclear Sci. Technol. 5 (2019) 17.

[76] P. German, M. E. Tano, J. C. Ragusa, Reduced-order modeling of coupled neutronics and fluid dynamics in the zero-power molten salt fast reactor, in: Proc. of Int. Conf. on Mathematics and Computational Methods Applied to Nuclear Science and Engineering (M&C 2021), 2021, p. 10 pp.

[77] R. Elzohery, J. Roberts, Modeling neutronic transients with galerkin projection onto a greedy-sampled, POD subspace, Annals of Nuclear Energy 162 (2021) 108–487.

[78] R. Elzohery, J. Roberts, Exploring transient, neutronic, reduced-order models using DMD/POD-Galerkin and data-driven DMD, EPJ Web Conf. 247 (2021) 15019.

[79] R. Elzohery, J. Roberts, A multiphysics reduced-order model for neutronic transient using POD-Galerkin projection and DEIM, Transactions of the American Nuclear Society 125 (2021) 440–443.

[80] T. R. F. Phillips, C. E. Heaney, B. S. Tollit, P. N. Smith, C. C. Pain, Reduced-order modelling with domain decomposition applied to multi-group neutron transport, Energies 14 (2021) 1369.

[81] A. S. Moore, T. M. Guymer, J. Morton, B. Williams, J. L. Kline, N. Bazin, C. Bently, S. Allan, K. Brent, A. J. Comley, K. Flippo, J. Cowan, J. M. Taccetti, K. Missack-Tamashiro, D. W. Schmidt, C. E. Hamilton, K. Obrey, N. E. Lanier, J. B. Workman, R. M. Stevenson, Characterization of supersonic radiation waves, Journal of Quantitative Spectroscopy & Radiative Transfer 159 (2015) 19–28.

[82] T. M. Guymer, A. S. Moore, J. Morton, J. L. Kline, S. Allan, N. Bazin, J. Benstead, C. Bentley, A. J. Comley, J. Cowan, K. Flippo, W. Garbett, C. Hamilton, N. E. Lanier, K. Mussack, K. Obrey, L.

Reed, D. W. Schmidt, R. M. Stevenson, J. M. Taccetti, J. Workman, Quantifying equation-of-state and opacity errors using integrated supersonic diffusive radiation flow experiments on the National Ignition Facility, Physics of Plasmas 22 (2015) 043303.

[83] C. L. Fryer, E. Dodd, W. Even, C. J. Fontes, C. Greeff, A. Hungerford, J. Kline, K. Mussack, I. Tregillis, J. B. Workman, J. Bernstead, T. M. Guymer, A. S. Moore and J. Morton, Uncertainties in radiation flow experiments, High Energy Density Physics 18 (2016) 45–54.

[84] C. L. Fryer, A. Diaw, C. J. Fontes, A. L. Hungerford, J. Kline, H. Johns, N. E. Lanier, S. Wood, T. Urbatsch, Designing radiation transport tests: Simulation-driven uncertainty-quantification of the COAX temperature diagnostic, High Energy Density Physics 35 (2020) 100738.

[85] V. Ya. Gol'din, A quasi-diffusion method of solving the kinetic equation, USSR Comp. Math. and Math. Phys. 4 (1964) 136–149.

[86] L. H. Auer, D. Mihalas, On the use of variable Eddington factors in non-LTE stellar atmospheres computations, Monthly Notices of the Royal Astronomical Society 149 (1970) 65–74.

[87] V. Ya. Gol'din, B. N. Chetverushkin, Methods of solving one-dimensional problems of radiation gas dynamics, USSR Comp. Math. and Math. Phys. 12 (1972) 177–189.

[88] V. Ya. Gol'din, On mathematical modeling of problems of non-equilibrium transfer in physical systems, in: Modern Problems of Mathematical Physics and Computational Mathematics, Nauka, Moscow, 1982, pp. 113–127. In Russian.

[89] D. Mihalas, B. Weibel-Mihalas, Foundation of Radiation Hydrodynamics, Oxford University Press, 1984.

[90] K.-H. A. Winkler, M. L. Norman and D. Mihalas, Implicit adaptive-grid radiation hydrodynamics, in: Multiple Time Scales, Academic Press, 1985, pp. 145–184.

[91] V. Ya. Gol'din, D. A. Gol'dina, A. V. Kolpakov, A. V. Shilkov, Mathematical modeling of hydrodynamics processes with high-energy density radiation, Problems of Atomic Sci. & Eng.: Methods and Codes for Numerical Solution of Math. Physics Problems 2 (1986) 59–88. In Russian.

[92] D. Y. Anistratov, E. N. Aristova, V. Y. Gol'din, A nonlinear method for solving problems of radiation transfer in a physical system, Mathematical Modeling 8 (1996) 3–28. In Russian.

[93] E. N. Aristova, V. Ya. Gol'din, A. V. Kolpakov, Multidimensional calculations of radiation transport by nonlinear quasi-diffusion method, in: Proc. of Int. Conf. on Math. and Comp., M&C 1999, Madrid, Spain, 1999, pp. 667–676.

[94] D.Y. Anistratov, V. Ya. Gol'din, Multilevel quasidiffusion methods for solving multigroup transport k-eigenvalue problems in one-dimensional slab geometry, Nuclear Science and Engineering 169 (2011) 111–132.

[95] A. Tamang, D.Y. Anistratov, A multilevel quasidiffusion method for solving space-time multigroup neutron kinetics equations coupled with the heat transfer equation, Nuclear Science and Engineering 177 (2014) 1–19.

[96] L. R. Cornejo, D. Y. Anistratov, The multilevel quasidiffusion method with multigrid in energy for eigenvalue transport problems, Progress in Nuclear Energy 101 (2017) 401–408.

[97] D. Y. Anistratov, Stability analysis of a multilevel quasidiffusion method for thermal radiative transfer problems, Journal of Computational Physics 376 (2019) 186–209.

[98] J. A. Fleck, J. D. Cummings, An implicit Monte Carlo scheme for calculating time and frequency dependent nonlinear radiation transport, J. of Comp. Phys. 8 (1971) 313–342.

[99] Y. B. Zeldovich, Y. P. Razier, Physics of Shock Waves and High Temperature Hydrodynamic Phenomena, Academic, New York, 1966.

[100] I. C. F. Ipsen, Numerical Matrix Analysis, Society for Industrial and Applied Mathematics, 2009.

[101] E. Smith, I. Variansyah, R. McClarren, Variable dynamic mode decomposition for estimating time eigenvalues in nuclear systems, arXiv preprint arXiv:2208.10942 (2022).

[102] B. Li, J. Garicano-Mena, E. Valero, A dynamic mode decomposition technique for the analysis of non–uniformly sampled flow data, Journal of Computational Physics 468 (2022) 111495.

[103] K. K. Chen, J. H. Tu, C. W. Rowley, Variants of dynamic mode decomposition: Boundary condition, Koopman, and Fourier analyses, Journal of Nonlinear Science 22 (2012) 887–915.

[104] A. Alla, J. N. Kutz, Nonlinear model order reduction via dynamic mode decomposition, SIAM J. Sci. Comput. 439 (2017) B778–B796.

[105] P. Ghassemi, D. Y. Anistratov, Multilevel quasidiffusion method with mixed-order time discretization for multigroup thermal radiative transfer problems, Journal of Computational Physics 409 (2020) 109315.

[106] M. L. Adams, Subcell balance methods for radiative transfer on arbitrary grids, Transport Theory & Statistical Physics 26 (1997) 385–431.

[107] L. K. Abu-Shumays, Angular quadratures for improved transport computations, Transport Theory & Statistical Physics 30 (2001) 169–204.

[108] J. M. Coale, D. Y. Anistratov, A reduced-order model for thermal radiative transfer problems based on multilevel quasidiffusion method, in: Proc. of Int. Conf. on Mathematics and Computational Methods Applied to Nuclear Science and Engineering (M&C 2019), Portland, OR, 2019, p. 10 pp.

[109] J. Borggaard, K. R. Pond, L. Zietsman, Parametric reduced order models using adaptive sampling and interpolation, IFAC Proceedings Volumes 47 (2014) 7773–7778. 19th IFAC World Congress.

[110] N. Goizueta, A. Wynn, R. Palacios, Adaptive sampling for interpolation of reduced-order aerolastic systems, AIAA Journal 60 (2022) 6183–62022.

[111] C. W. Rowley, J. E. Mardsen, Reconstruction equations and the Karhunen-Loève expansion for systems with symmetry, Physica D 142 (2000) 1–19.

[112] J. Reiss, P. Schulze, J. Sesterhenn and V. Mehrmann, The shifted proper orthogonal decomposition: A mode decomposition for multiple transport phenomena, SIAM Journal of Scientific Computing 40 (2018) A1322–A1344.